Report SAM-TR-79-9

② LEVEL

EXPERIMENTAL VALIDATION OF THERMAL RETINAL MODELS OF DAMAGE FROM LASER RADIATION

Ashley J. Welch, Ph.D.
Leslie A. Priebe, Ph.D.
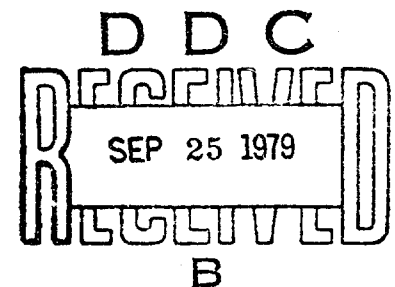Larry D. Forster, Ph.D.
Robert Gilbert, M.S.
Clement Lee, M.S.
Philip Drake
Bio-Medical Engineering Laboratory
The University of Texas
Austin, Texas 78712

August 1979

Final Report for Period August 1976 – April 1978

NOTICES

This final report was submitted by the Bio-Medical Engineering Laboratory, The University of Texas, Austin, Texas 78712, under contract F33615-76-C-0605, job order 7757-02-45, with the USAF School of Aerospace Medicine, Aerospace Medical Division, AFSC, Brooks Air Force Base, Texas. Captain Kenneth L. Schepler (SAM/RZL) was the Laboratory Project Scientist-in-Charge.

When U.S. Government drawings, specifications, or other data are used for any purpose other than a definitely related Government procurement operation, the Government thereby incurs no responsibility nor any obligation whatsoever; and the fact that the Government may have formulated, furnished, or in any way supplied the said drawings, specifications, or other data is not to be regarded by implication or otherwise, as in any manner licensing the holder or any other person or corporation, or conveying any rights or permission to manufacture, use, or sell any patented invention that may in any way be related thereto.

The animals involved in this study were procured, maintained, and used in accordance with the Animal Welfare Act of 1970 and the "Guide for the Care and Use of Laboratory Animals" prepared by the Institute of Laboratory Animal Resources - National Research Council.

This report has been reviewed by the Information Office (OI) and is releasable to the National Technical Information Service (NTIS). At NTIS, it will be available to the general public, including foreign nations.

This technical report has been reviewed and is approved for publication.

KENNETH L. SCHEPLER, Captain, USAF
Project Scientist

GARY E. VICE, Major, USAF
Supervisor

LAWRENCE J. ENDERS
Colonel, USAF, MC
Commander

REPORT DOCUMENTATION PAGE		READ INSTRUCTIONS BEFORE COMPLETING FORM
1. REPORT NUMBER SAM-TR-79-9	2. GOVT ACCESSION NO.	3. RECIPIENT'S CATALOG NUMBER
4. TITLE (and Subtitle) EXPERIMENTAL VALIDATION OF THERMAL RETINAL MODELS OF DAMAGE FROM LASER RADIATION.		5. TYPE OF REPORT & PERIOD COVERED Final Report. Aug 76–Apr 1978
		6. PERFORMING ORG. REPORT NUMBER BME1-1978
7. AUTHOR(s) Ashley J. Welch, Leslie A. Priebe, Larry D. Forster, Ph.D., Robert Gilbert, Clement Lee, M.S., Philip Drake, B.S.		8. CONTRACT OR GRANT NUMBER(s) F33615-76-C-0605
9. PERFORMING ORGANIZATION NAME AND ADDRESS Bio-Medical Engineering Laboratory The University of Texas Austin, Texas 78712		10. PROGRAM ELEMENT, PROJECT, TASK AREA & WORK UNIT NUMBERS 62202F 7757-02-45 02
11. CONTROLLING OFFICE NAME AND ADDRESS USAF School of Aerospace Medicine (RZL) Aerospace Medical Division (AFSC) Brooks Air Force Base, Texas 78235		12. REPORT DATE Aug 1979
		13. NUMBER OF PAGES 73
14. MONITORING AGENCY NAME & ADDRESS(if different from Controlling Office)		15. SECURITY CLASS. (of this report) Unclassified
		15a. DECLASSIFICATION/DOWNGRADING SCHEDULE

16. DISTRIBUTION STATEMENT (of this Report)

Approved for public release; distribution unlimited.

17. DISTRIBUTION STATEMENT (of the abstract entered in Block 20, if different from Report)

18. SUPPLEMENTARY NOTES

19. KEY WORDS (Continue on reverse side if necessary and identify by block number)

Eye, threshold, laser effects, temperature predictions.

20. ABSTRACT (Continue on reverse side if necessary and identify by block number)

This research concerns the validation of a model for the mathematical prediction of laser-radiation thermal damage on the eye. The model developed by IITRI for the Air Force has four distinct steps: (1) The laser image at the retina is computed. (2) The amount of heat generated by absorption of light in the pigment epithelium, choriocapillaris, and choroid is computed. (3) This heat is used in the linear heat-conduction equation to calculate the

DD FORM 1473 EDITION OF 1 NOV 65 IS OBSOLETE

UNCLASSIFIED

laser-induced temperature rise in the eye. (4) The potential of damage for any point in the fundus is found with a sequence of first-order rate process equations which use the computed temperature-time histories.)

The University of Texas conducted a series of dye cell and animal experiments for the purpose of validating the IITRI model. In the dye cell experiments, retinal absorption was modeled as a single homogeneous absorbing layer with known optical, thermal, and geometric parameters. Temperature measurements as a function of corneal power, wavelength, beam radius, beam distribution, and exposure duration were compared to predicted temperature. Experimental maximum temperature rises for all image sizes averaged 2% higher (with standard deviation of 29%) than model temperature for 30-ms argon radiation, 2% higher (SD=39%) for 10-s argon radiation, and 14% lower (SD=20%) for Nd-Yag radiation. The average agreement in the shape of experimental and model radial and axial profiles and the closeness of average measured and model maximum temperature rise validated the source term and temperature prediction sections of the model when the thermal and geometric parameters of a system are known.

In the second set of experiments we measured the retinal intensity profile, temperature rise, threshold power, and extent of damage as a function of wavelength, beam radius, intensity distribution, and exposure duration in the monkey eye. The thresholds determined were consistent with values reported in the literature. Measured maximum temperatures were typically one-half of model temperatures for image radii (as measured at the $1/e^2$ point) less than 150 μm. The radial profile of experimental temperatures, however, was much broader than model profiles. Differences between predicted and measured temperatures were attributed to incorrect absorption coefficients in the IITRI model and possible scattering of the laser beam in the absorbing layers. Since IITRI rate process coefficients were selected to correctly predict damage from the computed temperature profiles, the rate process section of the model underestimated predicted damage when calculations were based on experimental temperature rise.

Absorption and rate process coefficients should be redetermined for the model. If scattering takes place in the retina, its effects should be included in the model.

ACCESSION for	
NTIS	White Section
DDC	Buff Section ☐
UNANNOUNCED	☐
JUSTIFICATION	
BY	
DISTRIBUTION/AVAILABILITY CODES	
Dist.	AVAIL and/or SPECIAL
A	

TABLE OF CONTENTS

CONTENTS (continued)

LIST OF ILLUSTRATIONS

CONTENTS (continued)

LIST OF TABLES

EXPERIMENTAL VALIDATION OF THERMAL RETINAL
MODELS OF DAMAGE FROM LASER RADIATION

INTRODUCTION

In the early 1970's the Air Force foresaw the rapid development of laser systems and the need for establishing a long-range hazard evaluation program. It was apparent that a program based solely on experimental threshold determinations could not practically be used to set safety standards for each new laser system development. Anticipating this difficulty, the Air Force developed a model for the mathematical prediction of thermal effects of laser radiation on the eye (8). Given the characteristics of the laser such as wavelength, exposure duration, power, and divergence of the laser beam, the model was designed to compute temperature rise in the ocular media and the extent of damage; also to predict the power required to cause a specified extent of damage.

During the development phase of the model, the Air Force sponsored a series of experiments involving temperature measurement in the laser-irradiated eye (9,10,11). These experiments established the feasibility of the temperature model and provided data for optimizing the model. The experiments also demonstrated that it was possible to make accurate measurements of threshold temperature rise for a wide range of exposure durations. The measurement of temperature in the eye provided a means of experimentally validating predictions of the model for thermal damage (11).

The objective of this research is the experimental validation of the Air Force model for thermal damage in the laser-radiated eye. This is essential for establishing the accuracy and credibility of the model for laser hazard evaluation. The model combines temperature calculations with a rate process program to predict damage. The temperature-prediction portion of the model is validated by comparing experimental temperature-time histories in a simple dye cell and in the monkey eye to calculate temperature profiles. The rate process section of the model is evaluated by comparing the predicted power that would produce specified lesion radii to the power necessary to produce threshold damage in the eye and the size of the lesion. Direct comparison of experimental and theoretical values are made for intensity profiles, temperature histories, damage threshold, and the radial extent of damage.

The intensity profile and temperature measurements are made with microthermocouples (2). Threshold damage and the extent

of lesion radii are determined by microscopic examination of flat preparations of the fundus (11). Only animals with clear ocular media and normal fundi were used in the research.

All experiments were conducted in accordance with an experimental plan prepared by The University of Texas and approved by the Air Force. Specific tasks for this research were:

1. Intensity profiles and temperature-time histories in a simple dye cell were compared to values predicted by the thermal model. Retinal absorption was modeled in a dye cell with a single homogeneous absorbing layer of known optical, thermal, and geometrical properties. Intensity and temperature measurements were made as a function of corneal power, wavelength, beam radius, distribution, and exposure duration. The exact experimental conditions for the dye cell experiments are listed in Table 1.

2. Measurements of intensity profile, temperature rise, threshold exposure, and the extent of damage were made in the monkey eye as a function of corneal power, wavelength, image radius, distribution, exposure duration, and number of pulses. The exact experimental conditions are listed in Table 2.

TABLE 1. EXPERIMENTAL DYE CELL CONDITIONS

Condition	Pulse duration	Image radius* (µm)	Profile	Wavelength (nm)
1	30 ms	10	G	514.5
2	30 ms	100	G	514.5
3	30 ms	1000	G	514.5
4	10 s	10	G	514.5
5	10 s	100	G	514.5
6	10 s	1000	G	514.5
7	30 ms	10	G	1060.0
8	30 ms	100	G	1060.0
9	30 ms	1000	G	1060.0

* - Defined as $1/e^2$ radius of the intensity profile
G - Gaussian profile

6

TABLE 2. EXPERIMENTAL ANIMAL CONDITIONS

Condition	Pulse duration	Radius* (μm)	Profile	Wave-length (nm)	Inser-tion site
1	30 ms	min	G	514.5	M,P
2	10 s	min	G	514.5	M,P
3	30 ms	100	G	514.5	M,P
4	10 s	100	G	514.5	M,P
5	30 ms	1000	G	514.5	M,P
6	10 s	1000	G	514.5	M,P
7	30 ms	min	G	1060.0	M,P
8	10 s	min	G	1060.0	M,P
9	30 ms	100	G	1060.0	M,P
10	10 s	100	G	1060.0	M,P
11	200 ns	min	G	1060.0	M,P

*   - $1/e^2$ radius of the beam profile on the retina
min - minimum image experimentally attainable
G   - Gaussian profile
M   - macula; P - paramacula

3. Measured values of intensity profile, temperature rise, threshold, and the radial extent of damage were compared to corresponding values predicted by the IIT Research Institute (8) thermal model. Damage predictions were made for each experimental run.

4. The accuracy of the IITRI model and its suitability for predicting damage were determined by analysis of computer and experimental results.

The following sections of this report are organized according to the above specific tasks.

BACKGROUND

A model developed for the Air Force by IITRI predicts laser damage to the eye as a function of the power, exposure duration, wavelength, intensity profile, and divergence of the beam at the cornea. The model involves a four-step process as illustrated in Figure 1. First, the retinal-image intensity profile may be computed from the beam characteristics at the cornea. The algorithm includes a modulation transfer function for mapping the laser image onto the retina. This section of the program may be bypassed by directly entering the relative retinal intensity profile into the program.

Beam profile,
divergence, and
power at cornea

Optical transfer function

Beam profile on retina

Deposition of heat due to absorption of laser light.

Heat source term as a function of radial and axial position in the fundus

Computation of temperature time history.

Temperature as a function of time, radial position, and axial position in the fundus.

Damage predictions

(a) Extent of damage (if damage occurs) for given input power.

(b) Power required to produce damage at specified radial and axial positions.

Figure 1. Block diagram of the IITRI model for prediction of thermal damage in the laser-radiated eye.

Second, the program calculates the heat produced by laser-light absorption in the fundus. The algorithm assumes Beer's law of light absorption in the pigment epithelium (PE), chorio-capillaris, choroid, sclera, and tissue behind the sclera. First-order reflections at each tissue interface are considered in the algorithm. Since the melanin granules are concentrated in a narrow layer in the pigment epithelium, the PE may be divided into two separate layers. In the monkey eye the first one-third of the PE is highly absorbent, and the remaining two-thirds are assumed to have the same absorption as the choroid. Thickness of the absorbing layers, absorption coefficients, and the percent of light reflected from cornea and retina have been determined experimentally for both human and monkey eyes. From this data the Air Force has selected a set of values for the monkey for use in this research. (See Table 3.)

The absorption profile for the monkey fundus at a 514.5-nm wavelength is shown in Figure 2. From this we see that absorption of the laser radiation is primarily confined to the pigment epithelium. The illustration includes the effect of concentrated absorption of the melanin granules in the first one-third of the PE. The effective absorption coefficient for this narrow band is 4123 cm^{-1}. Effects of reflections and reabsorption are not considered in the figure.

Third, once the heat source has been computed, the heat-conduction equation is solved using the parameter values listed in Table 3. This solution includes the effects of blood flow upon the temperature rise. Temperature predictions from the IITRI temperature model have been compared to other computer solutions of the heat-conduction equation and to experimental data from a simple dye cell (11). Generally, computed and experimental results have been within ±15% when the thermal parameters of the experiments were known.

Fourth, the thermal model computes the damage function Ω (r,z) at radial (r) and axial (z) coordinates specified by the user. The axial coordinate corresponds to depth in the retinal tissues, while the radial coordinate specifies the distance from the center of the beam profile in the plane perpendicular to z. The rate process for thermal damage uses the entire computer temperature-time history $T(r,z,t)$ in degrees Kelvin from the on-set of laser radiation until the temperature returns to a normal baseline temperature. Coefficients in the damage integral are varied as a function of temperature, as indicated in equation 1.

$$\Omega(z,r) = c_1 \int e^{-c_2/T(r,z,t)}dt \tag{1}$$

where $c_1 = 0$ for $T \leq 316^\circ K$

$c_1 = 4.322 \times 10^{64}$ and $c_2 = 50{,}000$ for $316^\circ K < T \leq 323^\circ K$

$c_1 = 9.389 \times 10^{104}$ and $c_2 = 80{,}000$ for $T > 323^\circ K$

9

TABLE 3.   MODEL PARAMETERS FOR THE MONKEY EYE (8)

	Wavelength (nm)	
	$\lambda = 514.5$	$\lambda = 1060$
Transmission of ocular media	0.836	0.814
Absorption in cm^{-1}		
pigment epithelium	1485	363
choriocapillaris	166	108
choroid	166	108
sclera	166	108
Thickness in μm		
pigment epithelium	12	
choriocapillaris	10	
choroid	168	
sclera	1000	
Conductivity in cal/cm-s-^{0}C		
all layers	0.0015	
Specific heat of tissue in cal/g-^{0}C	1	
Specific heat of blood in cal/g-^{0}C	0.92	
Rate of blood flow in g/cm^{3}-s	0.001	
Reflection from		
cornea	0.025	0.025
retina	0.070	0.252
sclera	0.318	0.252
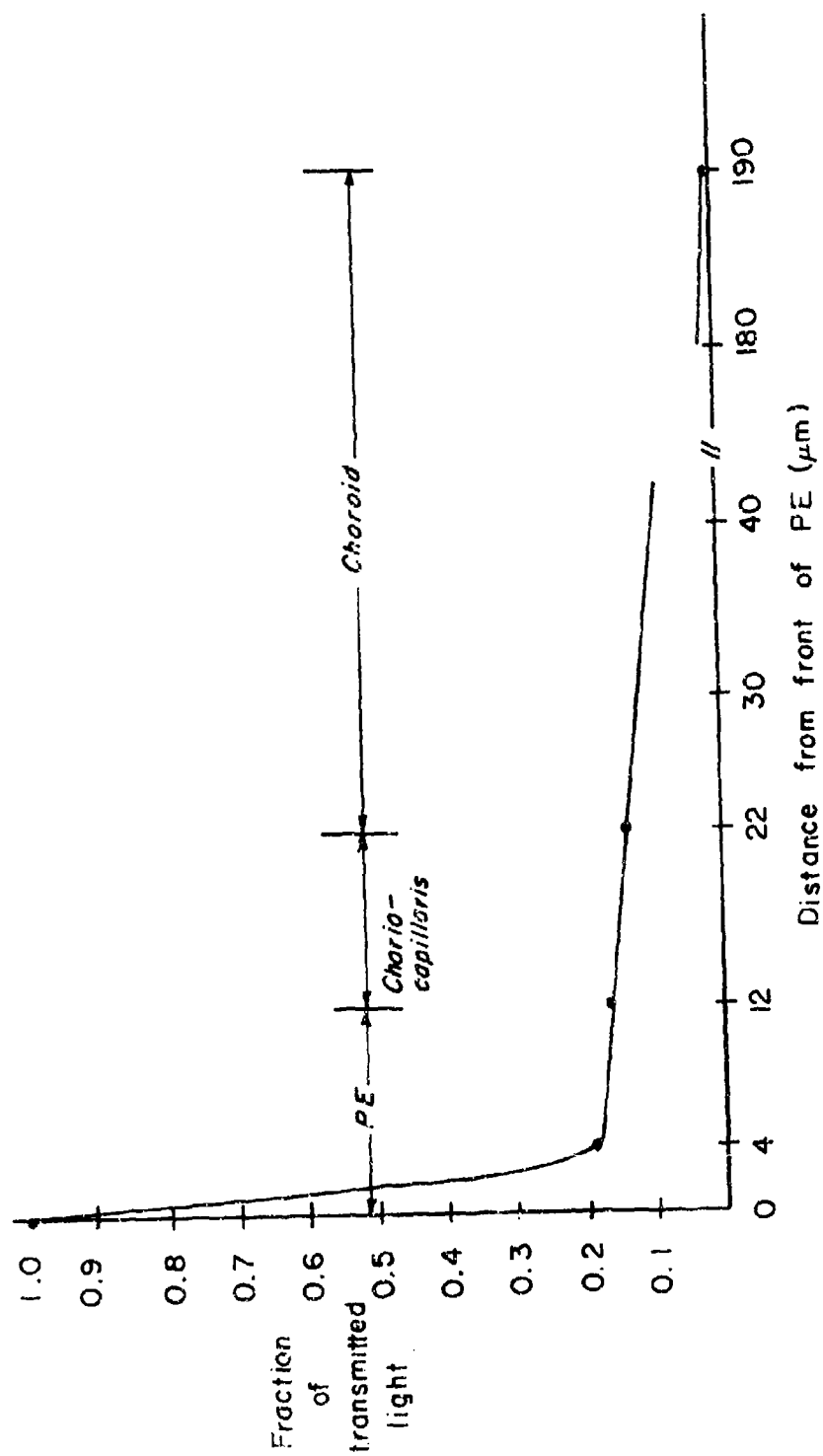
Figure 2. Absorption profile of monkey fundus for pigment epithelium, choriocapillaris, and choroid (514.5-nm wavelength).

Finally, the program rescales temperature profiles as a function of input power to predict the power required to create a specific lesion radius at certain depths.

PROCEDURE

Preexperimental Calibration

Several thermocouples were selected for use prior to each experiment. The thermoelectric EMF (electromotive force) of a thermocouple is determined by inserting it into a 37°C bath and heating the bath slowly to 80°C. Periodically, the voltage output of the thermocouple amplification system and the temperature of the bath are monitored. A plot of output voltage versus temperature yields a calibration value for the change in voltage per degree temperature change. This value is a function of the thermocouple, as well as the amplification system, and it represents a calibration factor for the entire system prior to each experiment.

The rise time of the thermocouple-tissue system is estimated by measuring the rise time of the temperature of the thermocouple, in a water environment, when irradiated directly with laser light. The laser beam is pulsed by a shutter, and the rise time (the time it takes the thermocouple to go from 10 to 90% of the actual temperature) is obtained. A second test is conducted for some thermocouples by noting the rise time when the tip of the probe is plunged into a hot bath.

The experimental rise time is a measure of the frequency response of the measurement amplifiers as well as the response time of the thermocouple to a step temperature increase. The time constant for a 20-μm diameter probe is approximately 0.5 ms (2).

The recording system is calibrated to determine if changes or failures have occurred by playing a calibration tape to check the playback electronics and by supplying a known calibration signal to test the record system. A calibration tape generated after the last recorder maintenance and calibration is played through the playback electronics. The output is checked for the proper output within ±2%. A known signal from a calibrator checks the attenuation and gain settings of the recorder preamplifier and the record system within ±2% at playback output.

Optical System

The optics for most dye cell and animal experiments consisted of a two-lens telescope (the first two lenses of the optical trains in Figure 3) and a third lens for converging the beam.

Lens A   Lens B   Lens C   Eye

Telescope   Lens–Eye Telescope

Lens E   Lens F   Lens G   Probe

Telescope   Dye Cell

* Adjust for desired image
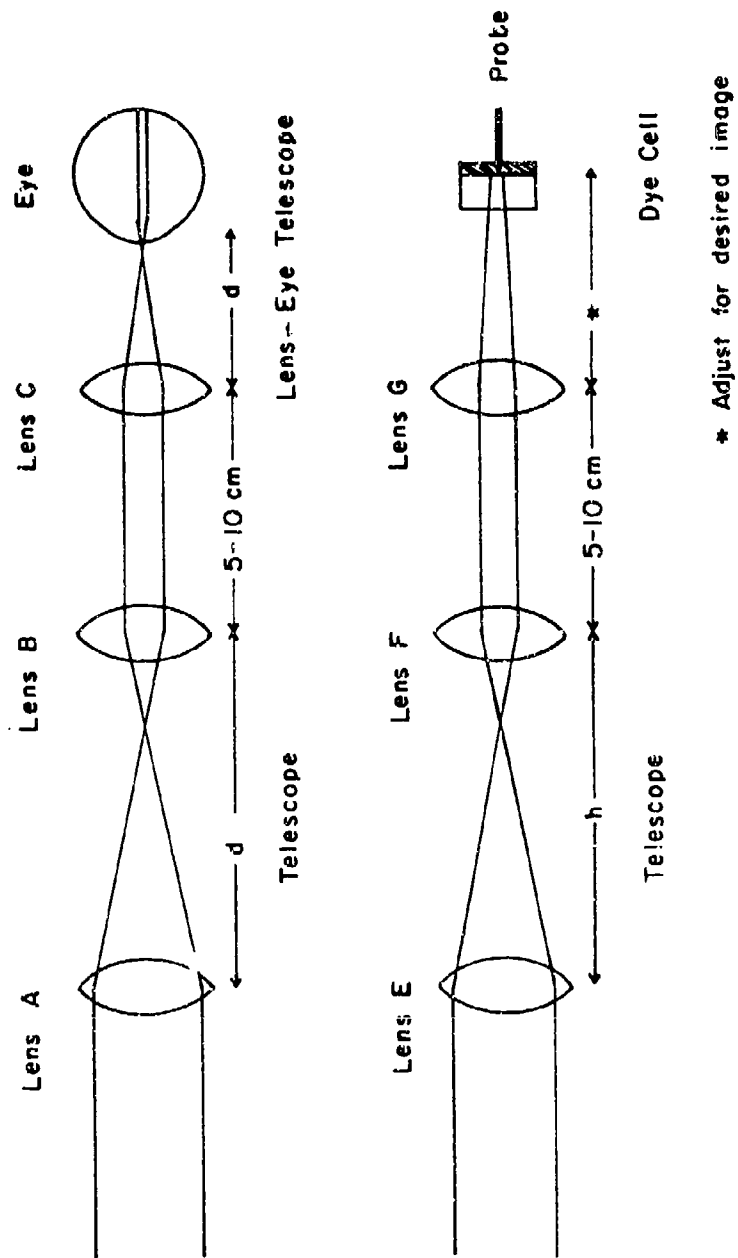
Figure 3. Optical configuration for animal and dye cell experiments.

13

Focal lengths of lenses and distances between lenses are given in Table 4. In the animal experiments, Lens C and the eye formed a second telescope which reduced the beam diameter by a factor of approximately 15 and minimized the divergence of the beam at the retina since the rays were approximately parallel after passing through the lens of the eye. The two-lens telescope reduced the beam diameter by a factor of 3 for the 100-μm and minimum spot images.

For the dye cell, the distance between the interface of the cell and the lens was adjusted to provide the desired image. The convergence of the beam at the interface was approximately 0.005 radians at the $1/e^2$ radius of the intensity profile.

TABLE 4. OPTICAL SYSTEM FOCAL LENGTHS AND DISTANCES

λ (nm)	Desired image $1/e^2$ radius (μm)	Eye Focal length (cm) A	B	C	Eye Distance (cm) d_1	d_2	Dye cell Focal length (cm) E	F	G	Dye cell Distance (cm) h
514.5	1000	5	20	30	25	32	5	20	30	25
514.5	100	20	5	30	25	32	20	5	30	25
514.5	min	20	5	*	25		20	5	30	25
1060.0	100	15	5	20	22	25	30	15	30	47
	min	15	5	*	22		30	15	30	47

min = minimum image
* Lens not used

Dye Cell Experiments

The dye was a mixture of Pelikan's 17 black water-soluble drawing ink and deionized water that was thickened by Matheson Coleman and Bell's bacteriological agar to form a gel medium. Ink was added until the darkness of the gel medium was about the same as the pigment epithelium of the eye. The medium was prepared by heating ink and water with agar powder at a temperature slightly below boiling for several minutes, as follows:

    0.75 cm³ ink
    4.25 cm³ water
    0.074 g agar (approximately).

The dye cell used for temperature measurement was a two-chamber cell consisting of a water chamber and a dye chamber (see Fig. 4). The water chamber was 18 mm thick and its diameter 25 mm, whereas the dye chamber was 5 mm thick and its diameter 10 mm. Both chambers were made of acrylic Plexiglas plastic, and they were mounted together with paraffin wax. In the front of the water chamber, a 0.2-mm-thick coverglass window was used
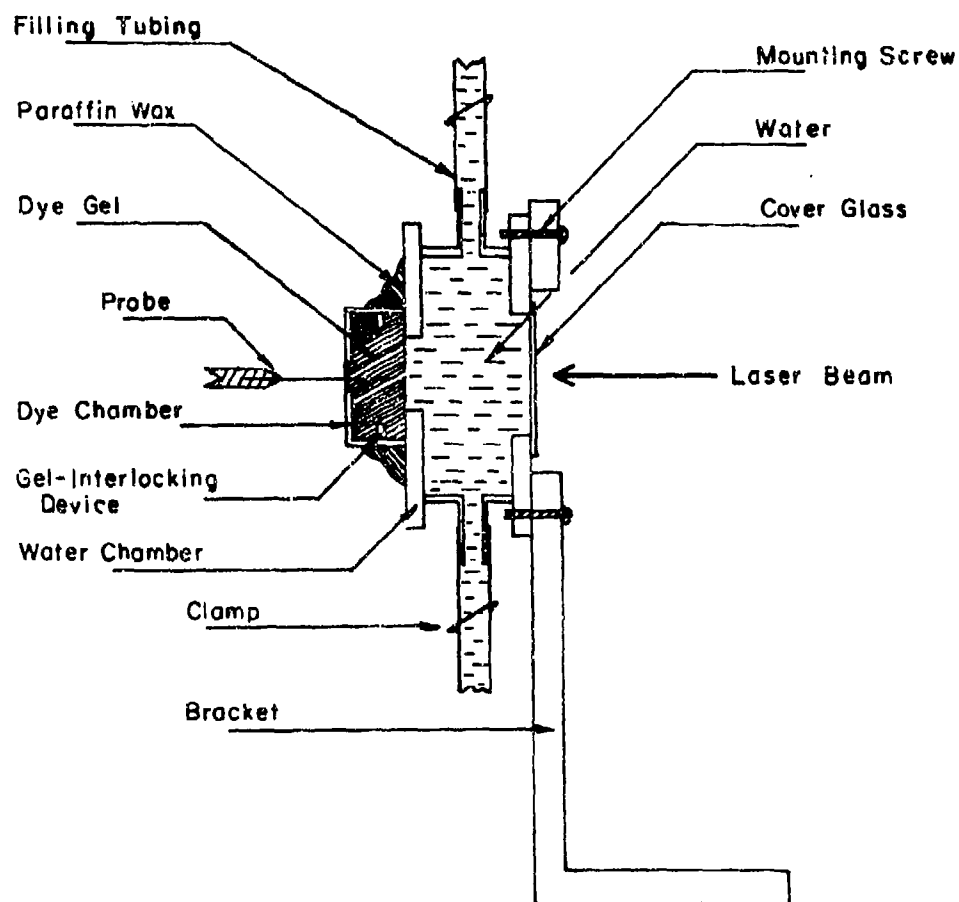
Figure 4. Two-chamber dye cell.

to allow the transmission of light; and at the back, a 9-mm-diameter opening was made for the interfacing of the water and gel media. A 2.5-mm-diameter probe was placed in the dye chamber for passing the thermocouple into the dye medium.

During gel preparation, the two chambers were taken apart. After the probe hole was temporarily sealed with a piece of tape, the dye chamber was filled with the warm gel solution. Before the gel solution had cooled down, its surface was smoothed out by a glass slide placed over the top of the dye chamber. The glass slide and the piece of tape were removed after the gel had hardened. Then the dye chamber was mounted with paraffin wax to the water chamber. The inlet and outlet tubings of the water chamber were clamped after it was filled with water. The water

chamber was held at a slight positive pressure to prevent bowing
of the gel-water interface. The whole device was mounted onto
the animal stereotaxic platform, with the center of the glass
window at the center of rotation of the platform (Fig. 5).
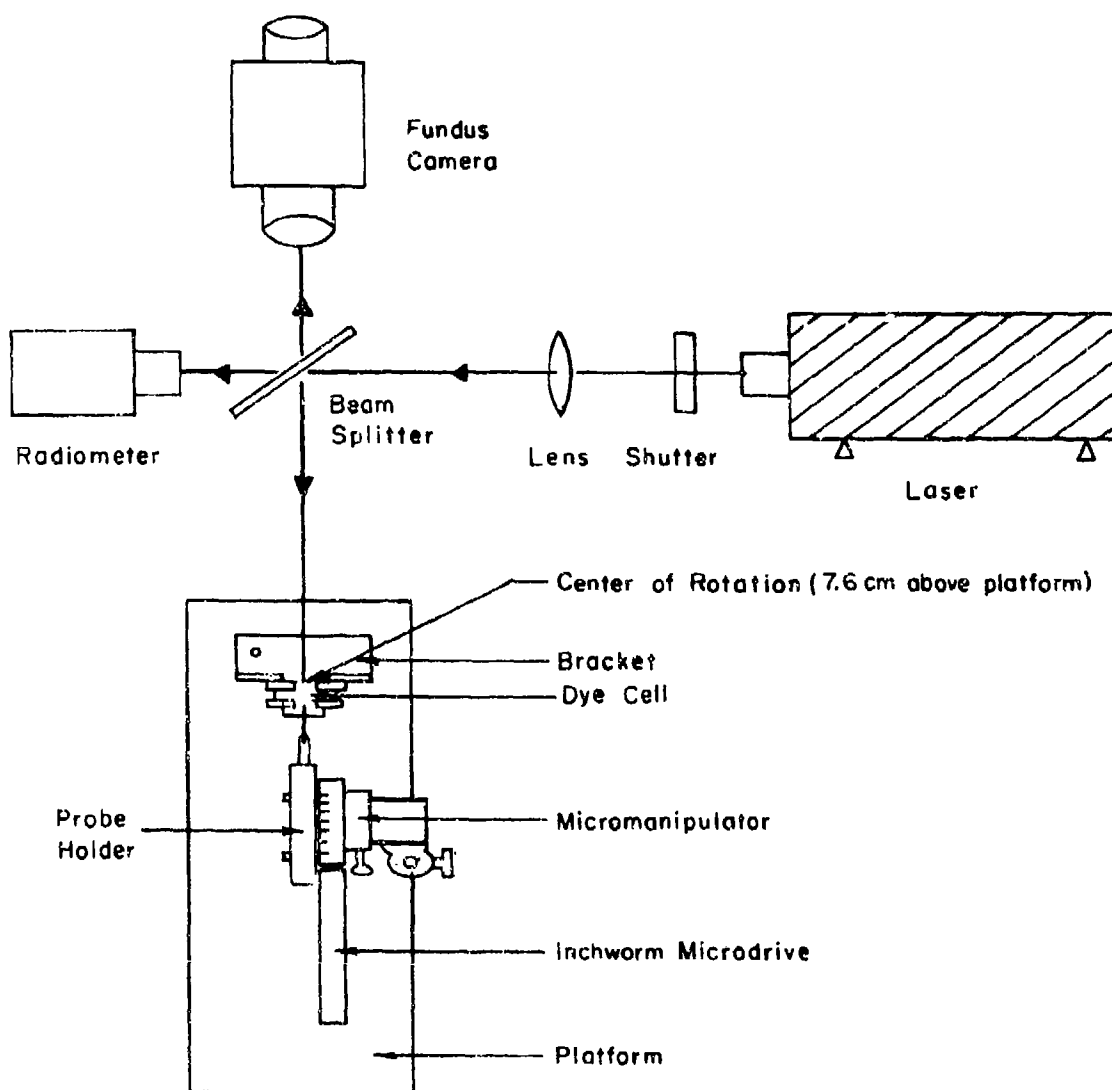
Figure 5. Relative location of equipment for dye
cell experiment.

The thermocouple was inserted into the dye cell through the probe hole by means of a micromanipulator at an angle normal to the interface, then was brought to a depth close to the interface by observing the position of the probe tip in the water chamber. When the probe was just visible, it was approximately 300 µm in front of the interface. The final axial adjustment of the probe position was accomplished with a Burleigh inchworm piezoelectric microdrive that had a resolution of 0.5 µm per step. The direct absorption characteristic of the thermocouple during 5-ms shuttered laser pulses was used to position the probe in the center of the beam (point of maximum temperature rise due to direct absorption). While the laser image remained fixed in space, the probe/dye-cell assembly was rotated in steps through the laser image to obtain a radial profile of the laser beam. Vertical rotation of the platform with a stepping motor provided profiles. The resolution of rotation was 16 arc seconds per step. This represented a 1.4-1.6-µm resolution per step at the interface, when the interface was 18 mm ±3% away from the point of rotation.

Based upon the direct absorption response of the thermocouple, the relative intensity profile of the laser beam was calculated. Using short (5 or 10 ms) pulses, the probe was retracted axially back into the gel to the point of maximum temperature rise in the center of the image. This hot spot in the gel was used as a reference point. From this point in the gel, radial temperature-time histories and profiles were measured at different depths, according to the experimental conditions specified in Table 1. They were recorded on a Clevite Brush, Mark 200, stripchart recorder and a Sangamo 3500 analog magnetic tape recorder for later computer analysis. Before the conclusion of the experiment, the radiometer reading of the average radiant laser power was recorded. Radiant power reaching the interface was calculated as the power at the surface of the cell times the measured transmission coefficient of the water-filled cell. Transmittance of the water chamber was defined as the fraction of radiant power incident on the radiometer which reached the water-gel interface.

The measured transmittance of the system was 0.931 for 514.5-nm and 0.570 for 1060-nm wavelengths. Laser radiation at wavelengths of 514.5 and 1060 nm was provided by a Spectra Physics 166 argon ion laser and a Chromatix 1000E Nd-Yag laser respectively.

The image size specified for a task in Table 1 was set up prior to each experiment. A fixed-lens system consisted of a two-lens telescope to collimate the laser beam and a long focal length (25 cm) lens to converge the image to the required size. Image size was checked by measuring the beam profile with the thermocouple.

Light absorption by the dye gel was measured using cells composed of two glass slides separated by a spacer approximately 0.2 mm thick. Five cells were filled with the same dye gel that filled the dye chamber. The spacer thickness of the dye layer of each cell was measured with a micrometer caliper. The absorption cell was mounted in front of the EG&G model 580 radiometer to measure light transmission. The light transmission reading of the cell with dye was compared to the measurement of a similar water-filled cell to minimize the effects of reflection and attenuation due to the glass layers of the cell.

Assuming light transmission was attenuated exponentially in the dye medium, the absorption coefficient, α, was calculated for each cell from the relation

$$\alpha = \frac{\ln(I_d/I_w)}{t} \tag{2}$$

where I_d was the light transmission through the dye-filled cell, I_w was the light transmission through the water-filled cell, and t was the thickness of the dye laser. All measurements were made with an accuracy of ±5%.

The transmission of the five dye samples was measured before and after each experiment. "Before" and "after" absorption coefficients were calculated for each cell. Since the difference between the two values was not significant, the mean of the two values was used as an average coefficient for the cell. Finally, the average coefficients of the five cells were again averaged to obtain the absorption coefficient used in the mathematical model.

The average absorption coefficient and measured values of the relative intensity profile, image radius, and power at the interface were used in the IITRI model to compute temperature profiles for the cell. The temperature rise in the gel was calculated with the IITRI multiple-layer model by setting the absorption coefficients of the pigment epithelium and choroid equal to the absorption coefficient of the gel. The conductivity of 0.0015 cal/(cm-s-°C) and specific heat of 1.0 cal/(g -°C) were used for all layers. All computation was done on a CDC 6600 digital computer at The University of Texas Computation Center.

Animal Experiments

Adult monkeys (Macaca mulatta) weighing 2-4 kg, supplied by the USAF School of Aerospace Medicine, were anesthetized and secured on an animal platform with ear bars. The backside of the left eye was exposed using a surgical procedure that removed sections of the skull, brain tissue, fascia, muscle, bony orbit, and periorbital fat and the lacrimal gland. (See reference 7 for more detail.) The sclera was then cleared of all fascia and the conjunctiva was sutured to an eye holder.

Upon completion of the surgery, the platform was attached to a five-degree-of-freedom animal holder and the eye was aligned with the fundus camera and laser (Fig. 6). A thermocouple with tip diameter of 10-20 μm was inserted through the macula into the vitreous humor. When it was 100-200 μm anterior to the pigment epithelium, the probe tip could be seen with the aid of the fundus camera. With the probe tip in the vitreous humor, the eye was irradiated with short, low-power laser pulses. The animal was positioned at the center of the beam (position of maximum direct-absorption rise in the thermocouple). The animal and probe were rotated through the laser beam in 25-100 μm radial steps, depending upon image size. At each step the intensity of the short laser pulse was measured in terms of the direct-absorption temperature rise of the thermocouple. The $1/e^2$ radius of the resulting intensity profile was measured. If the radius did not conform to the radius of the experimental test condition, the optics were adjusted and a new profile was measured.

After the intensity profile had been measured, the probe was retracted into the pigment epithelium to the layer that gave the highest temperature rise not including direct absorption for 30-msec pulsewidth irradiation. Radial and axial temperature-time histories were recorded on analog magnetic tape for the particular test conditions. The system bandwidth for thermocouple measurements was D.C. to 10 kHz, and the measurement error was estimated to be ±0.2°C.

Laser power was measured with an EG&G model 580 radiometer. After a patch was placed over the animal's eye, the shutter in the laser beam was opened and the continuous wave power was read from the radiometer.

When temperature measurements had been completed, the laser image was moved to macular tissue near the probe insertion site and a marker lesion was placed on the fundus. This lesion was followed by a series of decreasing power irradiations placed in rows of five to eight exposures with respect to the marker. Generally, the power of the laser was reduced by 5-10% between exposures. The position of each new row was indicated with a marker lesion. After completing the threshold series in the left eye, the platform was repositioned on the animal holder and a threshold series was placed in the right eye. The occurrences of ophthalmoscopically visible lesions were noted at 5 minutes and at 1 and 3 hours post exposure, when possible.

If the left eye was still clear at this point in the experiment, the probe was removed from the macular region and reinserted into the paramacula, temporal and/or superior to the macula. The temperature measurement and threshold series were then repeated. When measurements and threshold series were completed, the animal was sacrificed with an overdose of Nembutal and the eyes removed.

Both eyes were dissected and sections containing the lesions were removed. The neural layers were stripped from the fundus.
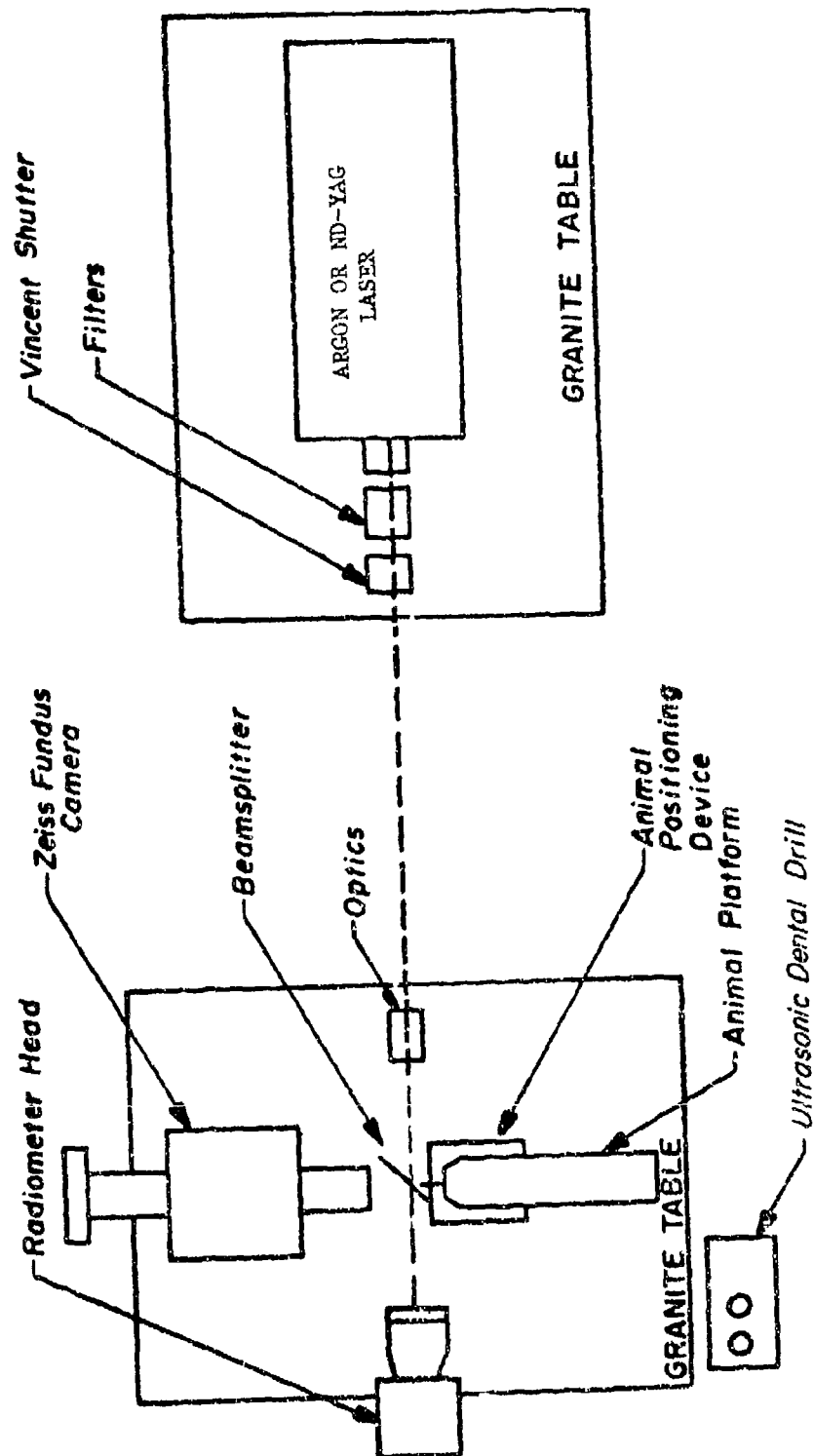
FIGURE 6: Laboratory arrangement of instruments.

Vincent Shutter

Filters

ARGON OR ND-YAG LASER

GRANITE TABLE

Radiometer Head

Zeiss Fundus Camera

Beamsplitter

Optics

Animal Positioning Device

Animal Platform

Ultrasonic Dental Drill

GRANITE TABLE

20

Next, the pigment epithelium and portions of the choroid were re-
moved. The section of the fundus containing the burn matrix was
bathed in Formalin for at least 2 hours, then placed on a micro-
scope slide. A cover glass was placed over the tissue, and the
cover glass and slide were sealed together with a 5-minute epoxy.
No noticeable shrinkage occurred. The flat mount of the irradi-
ated pigment epithelium was examined and photographed under a
light microscope at 35 and 100 power. Lesion diameters were
measured with the reticle located in the microscope eyepiece.
The minimum power required to produce a discernible lesion in a
threshold series was designated as the threshold power. The
extent of radial damage produced by this radiation was the thresh-
old lesion radius.

RESULTS

Dye Cell Experiments

The $1/e^2$ power radius, average absorption coefficient, ex-
posure power, probe size, and probe sensitivity of each experi-
ment are tabulated in Table A-1 of Appendix A. The $1/e^2$ power
radius is obtained from a plot of the irradiance profile that
is measured at the water/dye interface. This is the radius at
which the intensity has dropped to $1/e^2$ of its peak value. The
probe sensitivity is the thermoelectric EMF of the probe per $°C$.
The measured intensity profiles are represented by relatively
smooth profiles in the temperature model. An example of these
profiles is shown in Figure 7. With conductivity and the vol-
umetric specific heat specified to be 0.0015 cal/cm-s-$°C$ and
1.0 cal/(g-$°C$), respectively, computed temperatures were ob-
tained for the measured parameters of each experiment. A typical
time history of the response at the center of the profile is
shown in Figure 8. Radial temperatures after 0.01 s and 0.03 s
of argon laser irradiation are illustrated in Figure 9. Radial
temperatures 0.01 s and 0.05 s after irradiation stops are shown
in Figure 10.

A summary of experimental and model temperatures at the cen-
ter of the image and 1/2 power radius as a function of $1/e^2$
power radius, power, and probe depth, for the 514.5-nm radiations,
is presented in Table A-2 of Appendix A. Similar data at
1060 nm is presented in Table A-3. The data has been grouped
according to pulse duration and image size.

Results from different experiments are compared by normaliz-
ing maximum measured temperatures to an irradiation power of
1 mW. The maximum temperature rise at the beam center vs image
radius is illustrated in Figure 11 for 30-ms and 10-s exposures
at an argon wavelength of 514.5 nm. The data for 30-ms Nd-Yag
($\lambda=1060$ nm) radiation is shown in Figure 12. Curves in the
figures were drawn to best fit the temperature rise calculated
with the model for each experiment.

21
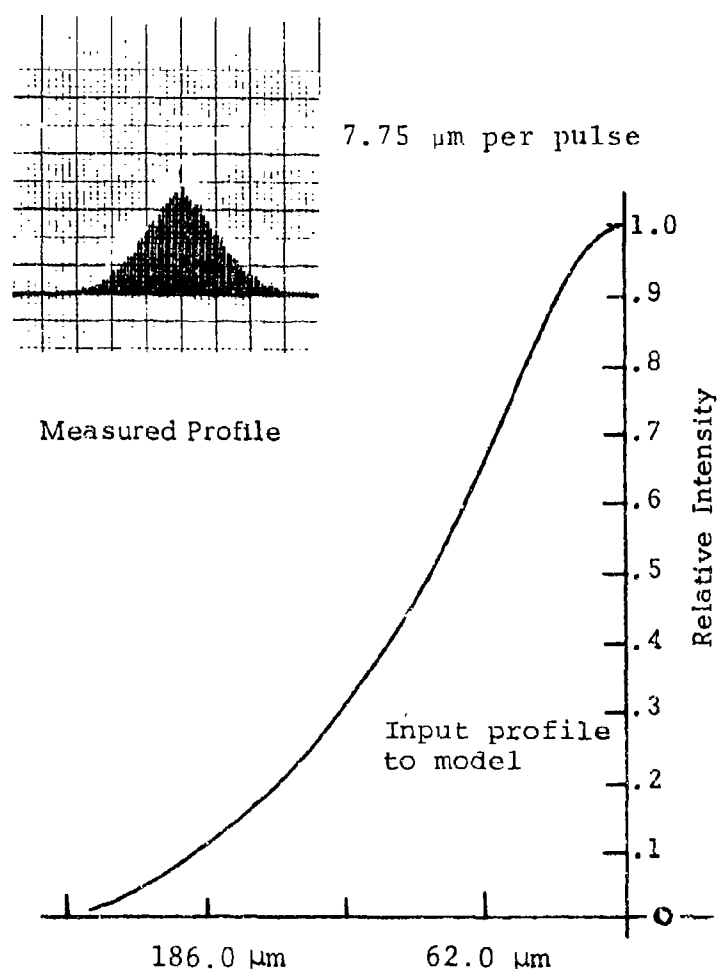
Figure 7. Measured and model relative-
intensity profile for dye cell.
(λ = 514.5 nm; $1/e^2$ power
radius = 172.5 μm).

Experimental maximum temperature rises for all image sizes
were on an average 2% higher (SD=29%) than model temperatures for
30-ms argon radiation, 2% higher (SD=39%) for 10-s argon radiation,
and 14% lower (SD=20%) for Nd-Yag radiation. At the half-power
radius the experimental temperature rises averaged 1% (SD=23%)
above computed temperatures for 30-ms argon, 5% (SD=21%) above for
10-s argon, and 13% lower (SD=20%) for Nd-Yag radiation. These
averages were c lculated from the tabulated results of Tables A-2
and A-3. If excreme differences were eliminated from the averages,
the standard deviations would improve from 5 to 10 percentage
points without affecting the average values.

λ = 514.5 nm, 30-ms exposure

Power = 13.98 mW

$1/e^2$ power radius = 172.5 μm

TIME (s)

TIME RISE (°C)
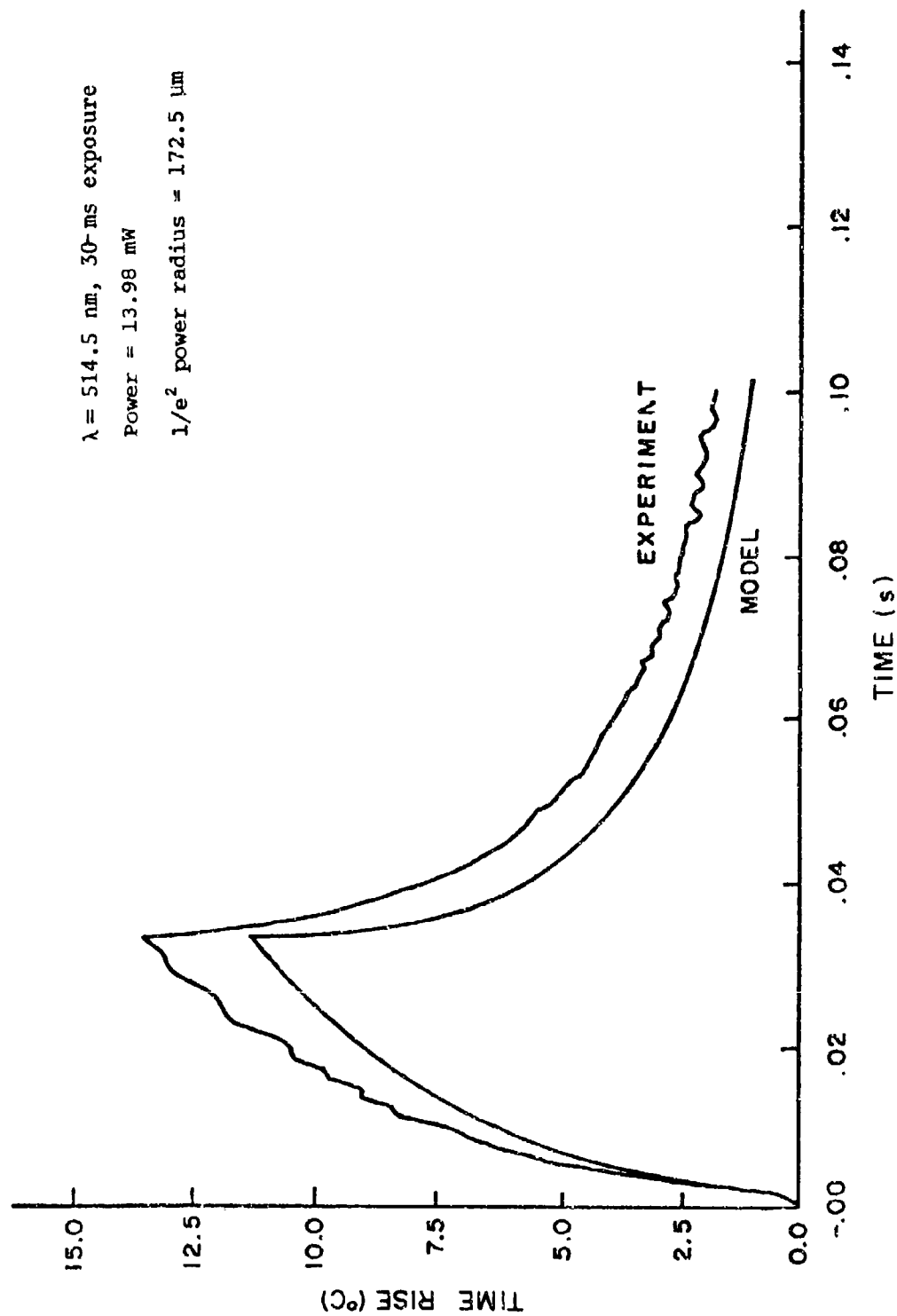
Figure 8. Experimental and model responses at the center of the temperature profile of Figure 7.
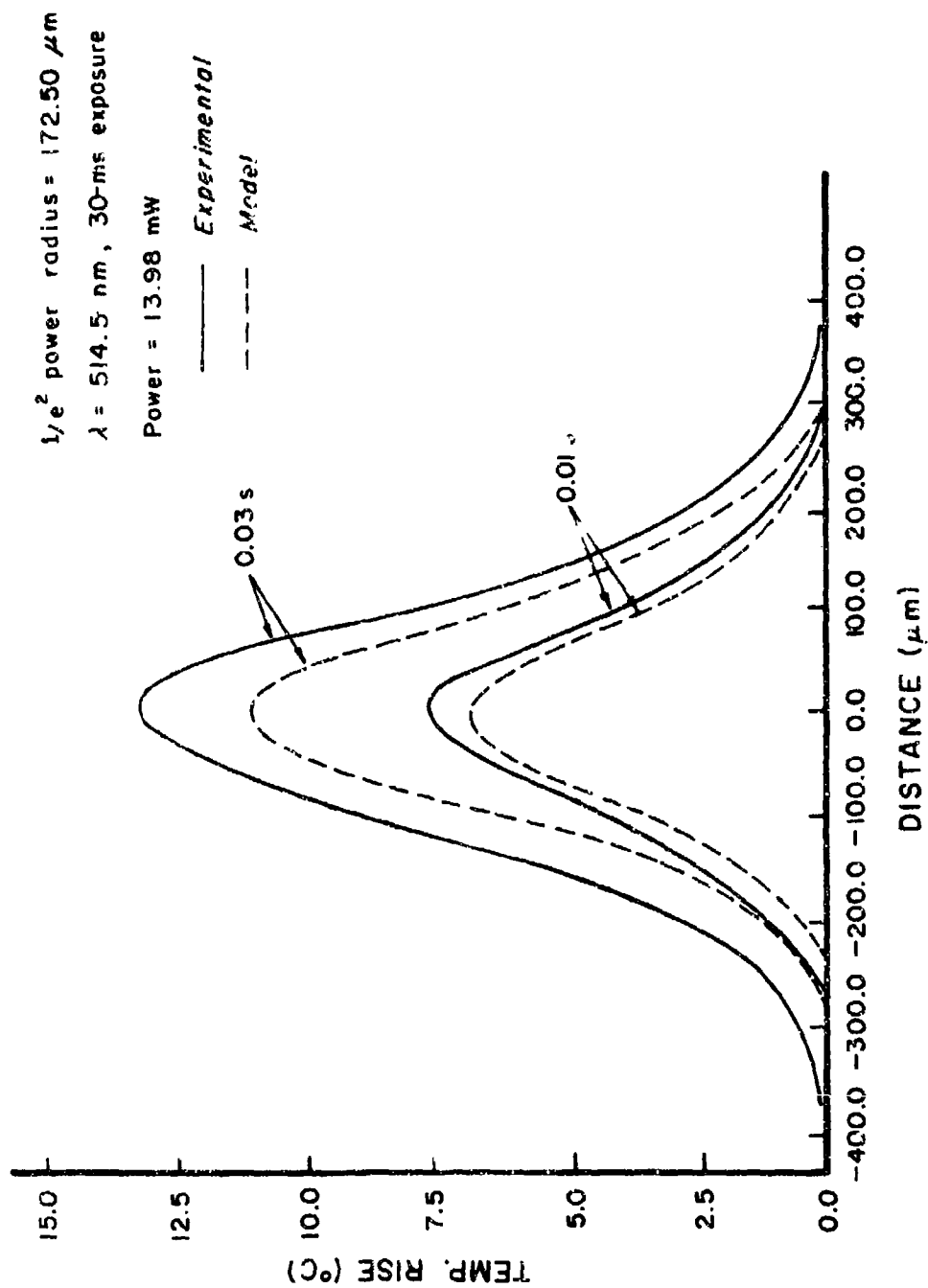
Figure 9. Experimental and model temperature (hot spot) radial profile during laser irradiation. Times indicated are elapsed times after irradiation began.
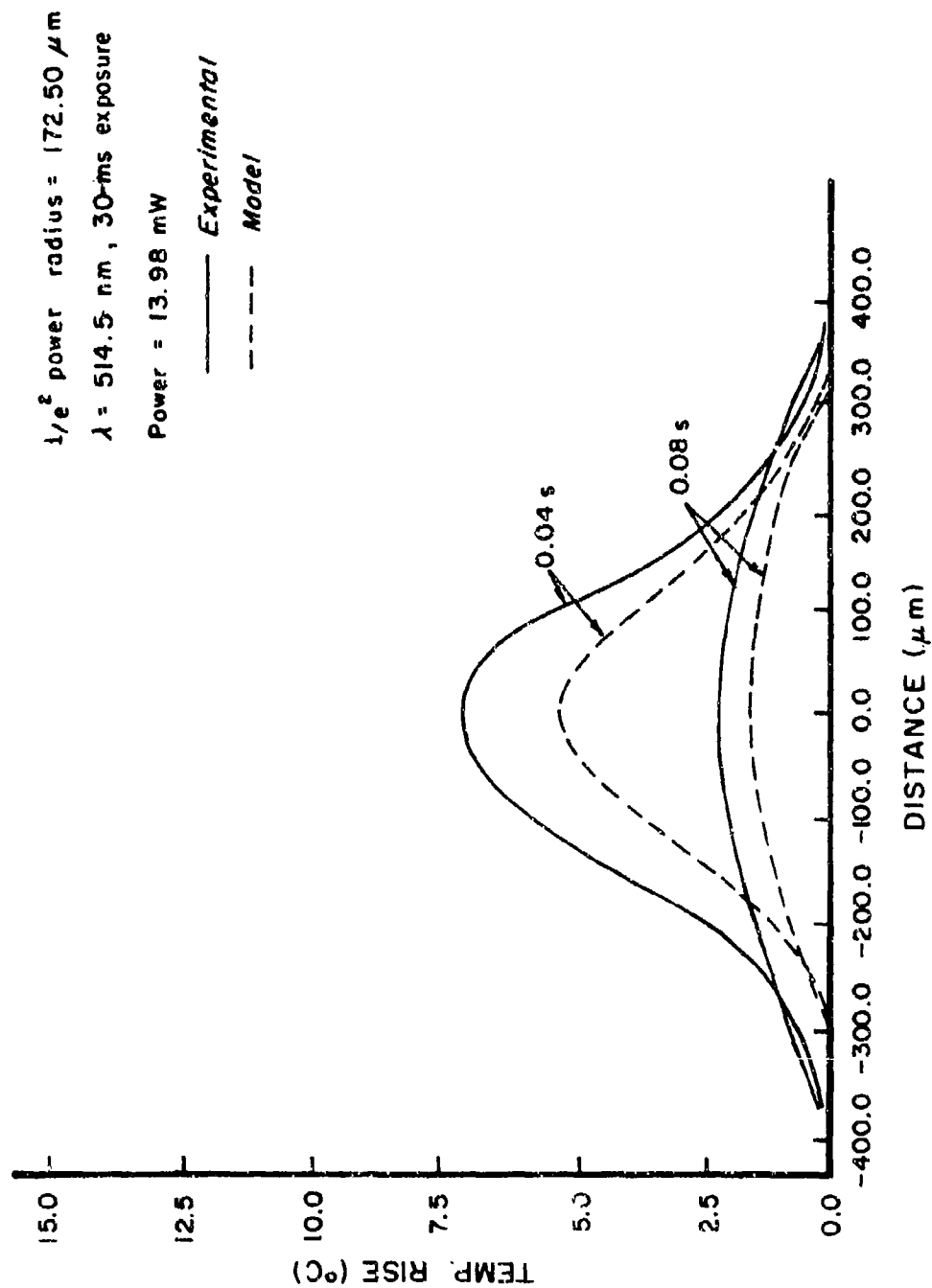
Figure 10. Experimental and model temperature (hot spot) radial
profile after laser irradiation. Times indicated are
elapsed times after irradiation began.
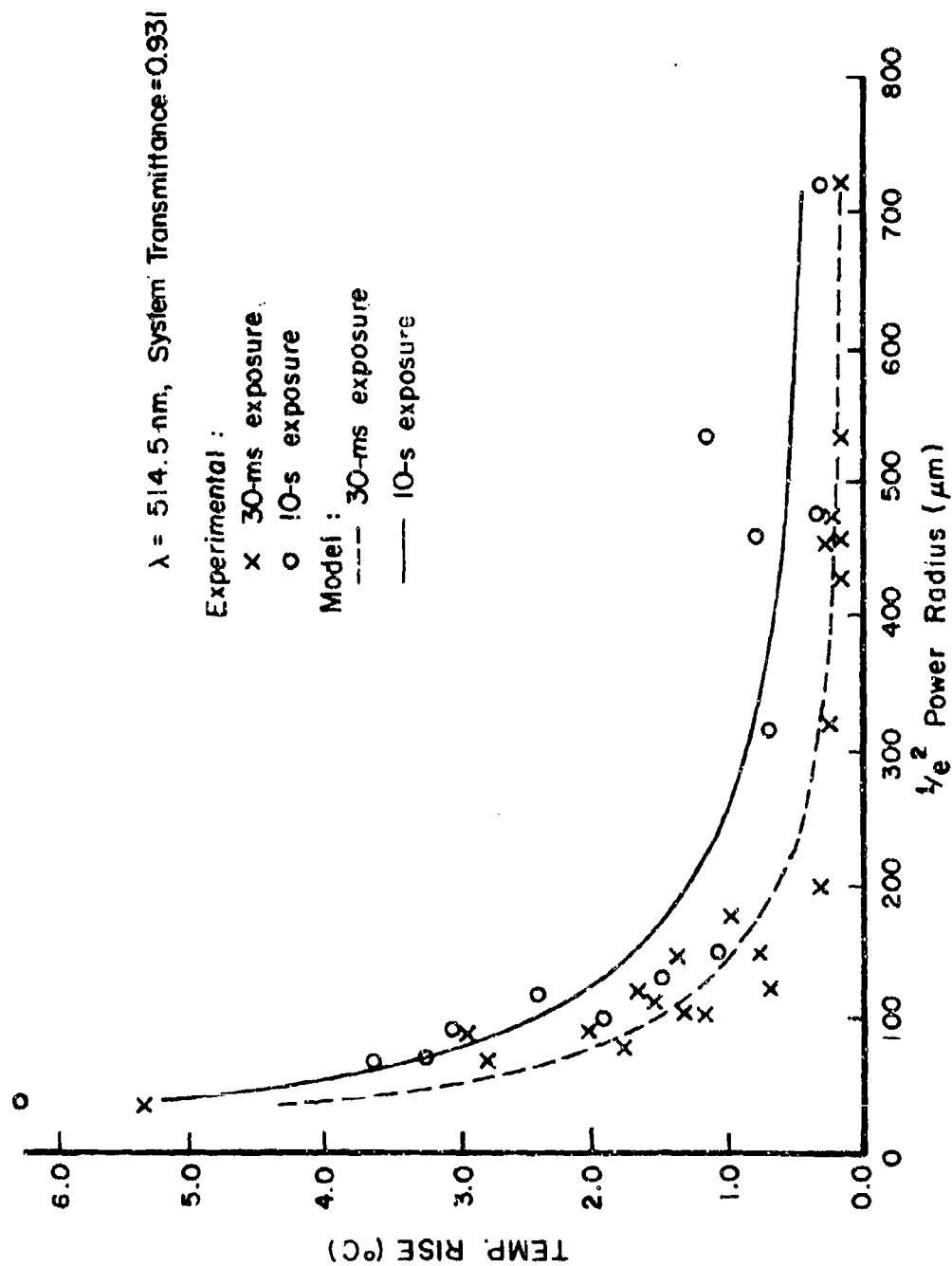
Figure 11. Temperature versus image radius for normalized argon irradiation of 1 mW.
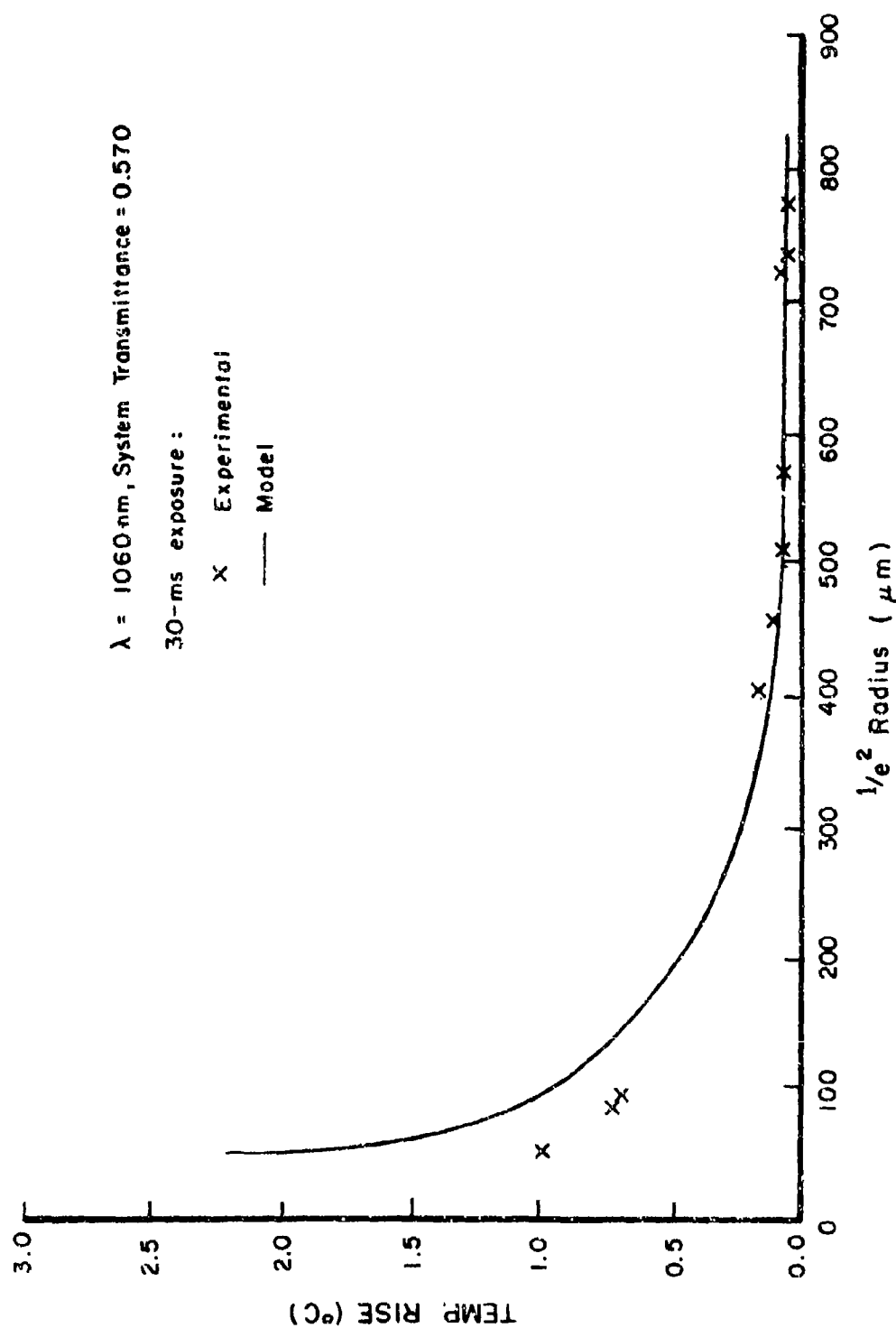
Figure 12. Temperature versus image radius for normalized Nd-Yag irradiation of 1 mW.

The shapes of the radial temperature profiles for all image radii were compared by normalizing the maximum temperature rise at the 1/2 power radius to the maximum temperature in the center of the beam. Normalized values of experimental and model temperatures computed from data in Tables A-2 and A-3 (Appendix A) are listed in Table A-4. For both the 514.5- and 1060-nm wavelengths, the average normalized experimental temperatures at the 1/2 power radius were slightly higher than the average of normalized model temperatures. The average percent difference for the 30-ms 514.5-nm experiments was 2.3% (SD=16%); for the 10-s 514.5-nm experiments, 7.3% (SD=16%); and for the 30-ms 1060-nm experiments, 1.5% (SD=5%).

The shapes of axial temperature profiles along the center line of the image were compared by normalizing the axial temperatures of Tables A-2 and A-3 with respect to the maximum hot-spot temperatures. The normalized experimental and model temperatures are listed in Table A-5. When questionable data with error values that exceeded 80% were neglected, the average errors between normalized experimental and model temperatures were 5.7% (SD=22%) for 30-ms argon and -4.3% (SD=24%) for 10-s argon radiation.

The average agreement in the shape of experimental and model radial and axial profiles, and the closeness of measured and model maximum temperature rises, indicated that the total energy deposition in the dye cell matched the energy deposition of the model.

Animal Experiments

Measured and calculated data for each experiment appear in Appendix A in Tables A-6—A-8. Experimental conditions such as animal identity, $1/e^2$ radius of the laser image, which eye was irradiated, and thermocouple location in left eye are listed with the experimental data. Experimental data in the tables consist of corneal threshold powers needed to produce ophthalmoscopically visible lesions (OVL) and microscopically visible lesions (MVL), lesion radii for the MVL thresholds, and the maximum temperature rises at the center of the image for OVL and MVL irradiations. Threshold temperatures are calculated from temperatures measured at subthreshold radiations by assuming a linear relation between temperature and power. That is

$$\frac{T(\text{at subthreshold corneal power})}{\text{Subthreshold corneal power}} = \frac{T(\text{at threshold corneal power})}{\text{Threshold corneal power}} \quad (3)$$

We use this relation to compute threshold temperatures in both the right and left eyes, based upon temperature measurements made in the left eye.

The maximum temperatures at the beam center predicted by the model for the MVL threshold power and the predicted lesion radius are also included in Tables A-6—A-8. If MVL threshold power was not available, then OVL threshold power was used for the model calculations.

The position of the probe, either macula (M) or paramacula (P), is given in the tables. All paramacular measurement sites were superior or temporal to the macula of the left eye. All macular measurements were made in the macula of the left eye. The eye for which the data are tabulated is listed as R (right) or L (left). No temperature measurements were made in the right eye; left-eye temperature measurements were used to estimate right-eye temperature increases. The same optics were used for both left and right eye exposures. Temperature values reported for the right eye assume that the beam profile for the macular or paramacular exposure was the same as the profile taken in the same area of the left eye.

Temperature Measurements as a Function of Image Size and Wavelength

Temperature measurements from different experiments are compared by normalizing maximum measured temperatures to an irradiation power of 1 mW. Normalized data for argon irradiation appear in Table A-9. The maximum temperature rise per mW vs image radius is shown in Figure 13 for 30-ms and in Figure 14 for 10-s argon (λ=514.5 nm) irradiation. Data from experiments where the eye blanched or notes indicated the data was bad were not included in the figures. The model temperatures for Gaussian profiles with the same $1/e^2$ radius are represented by the solid curve in each figure. The solid curve also represents the temperature rise per mW predicted for absorption coefficients of the pigment epithelium and choroid of 1485 cm^{-1} and 166 cm^{-1} respectively. The model temperatures were calculated with a model that has twice as many radial and axial grid points as the IITRI model. This model, which was supplied to the University by Mr. Tom White, will be designated in the remainder of this report as the UT model. The additional grid points of the UT model allow more accurate determination of model temperatures. (For a detailed comparison of the two models, see ref. 11.) The dashed curves on Figures 13 and 14 represent UT-model values when the absorption coefficients of the pigment epithelium and choroid are both set equal to 250 cm^{-1}. The last curve indicates the additional effect of having a source term that is 32 μm larger than the specified $1/e^2$ image radius and keeping the absorption coefficients at 250 cm^{-1}. The measured temperatures are 85% (SD=68%) higher than model values for 10-s Nd-Yag radiation.

The shapes of the radial temperature profiles are compared by normalizing the maximum temperature rise at the $1/e^2$ radius

29
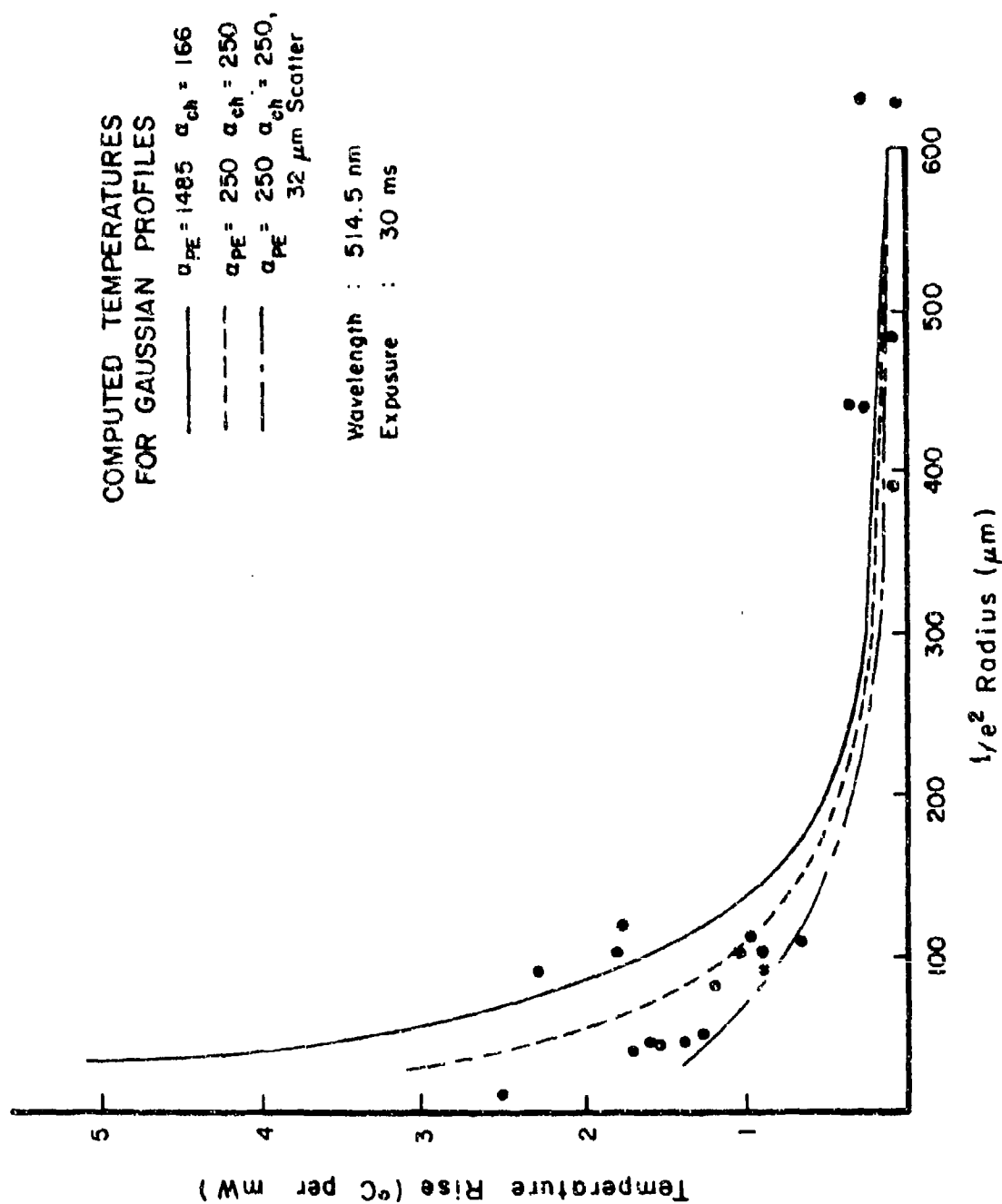
Figure 13. Temperature rise in monkey eye vs image radius for normalized argon irradiation of 1 mW.
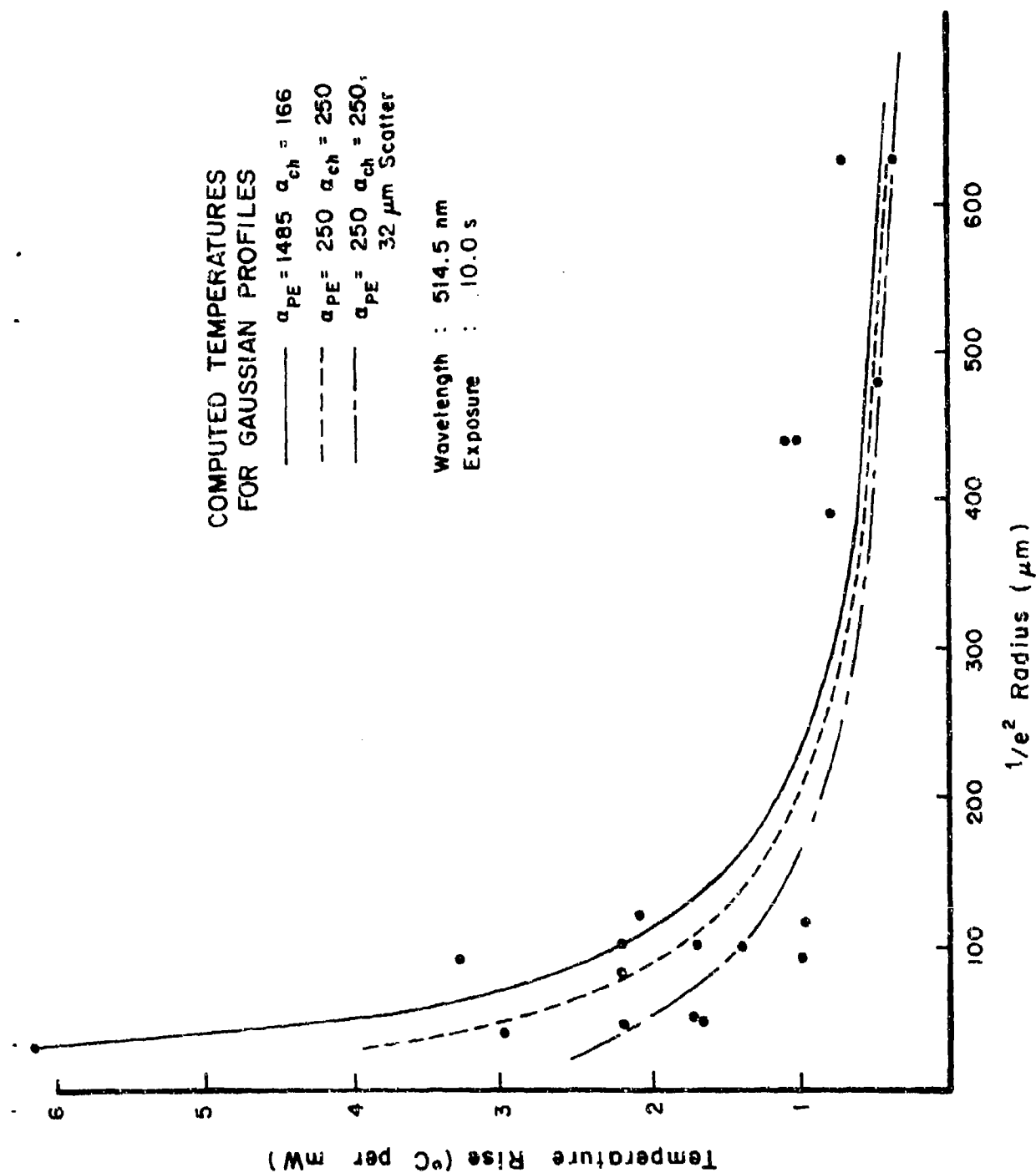
Figure 14. Temperature rise in monkey eye vs image radius for normalized argon irradiation of 1 mW.

to the maximum temperature in the center of the beam. Normalized
values of experimental temperatures for argon radiation are listed
in Table A-9. Ratios of temperature at $1/e^2$ radius to center tem-
peratures are shown in Figures 15 and 16 for 30-ms and 10-s argon
radiation. The solid curve was obtained with the UT model for a
Gaussian profile. The dashed curve illustrates the spreading
of the profile when both absorption coefficients are set equal
to 250 cm^{-1}, and the top curve depicts the additional effect of
scattering. Ratios for the scattering curve are based on an
assumption that scattering causes the laser energy to be deposited
in a profile 32 μm larger than the specified $1/e^2$ radius of the
beam profile measured in front of the retinal tissue.

Ratios of temperature at the $1/e^2$ radius to maximum center
temperature were computed from the data of Table A-10 for 30-ms
and 10-s Nd-Yag radiation. Averages of the model and experimen-
tal ratios for 30-ms radiations were 0.28 (SD=0.07) and 0.64
(SD=0.04) respectively. For 10-s radiation the average ratios
were 0.44 (SD=0.06) for the model and 0.79 (SD=0.12) for the
experimental values.

Comparison of Right- and Left-Eye Data

A comparison of right- and left-eye threshold corneal power
for argon radiation is presented in Table A-1. For the values
listed in the table, the average threshold powers for left and
right eye are 7.2 mW and 8.01 mW, respectively, for 10-s radia-
tion, and 21.5 mW and 25.4 mW for 30-ms radiation. T-tests in-
dicate there is no significant difference between threshold
powers for the left and right eye.

Comparison of MVL and OVL Thresholds

Ratios of MVL threshold power to OVL threshold power were
computed for the data of Tables A-6—A-8. Except for one Nd-Yag
data point that was omitted from the averages, the MVL threshold
was always less than or equal to the OVL threshold. The ratio
for 30-ms and 10-s argon radiation was 0.78 (SD=0.16) and 0.72
(SD=0.17) respectively. The ratio was 0.91 (SD=0.1) for 10-s
Nd-Yag radiation. The Nd-Yag laser did not have sufficient power
to produce OVL lesions for the 30-ms exposures.

Measurements of Lesion Radii and Lesion-Radius-Temperature Increases

Measured temperature increase at the lesion radius vs lesion
radius was obtained for a number of 10-s and 30-ms argon irradia-
tions. Microscopic measurements of lesion radii were made from the
flat preparation of the pigment epithelium.

Figure 17 illustrates the dependence of lesion radius on supra-
threshold corneal power. The solid lines in the figure represent
the IITRI-model predicted lesion radius values as a function of
corneal power. The zero lesion radius indicates "no damage."
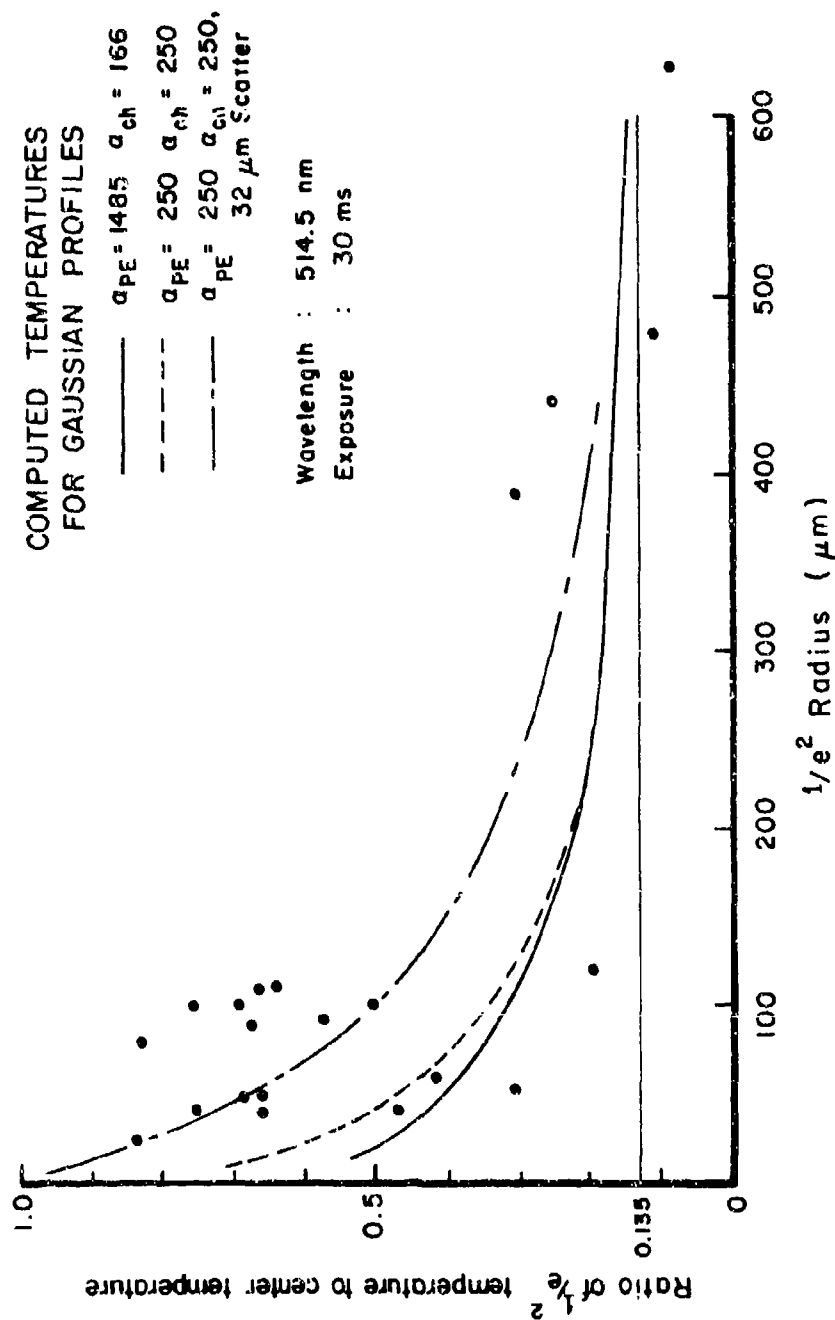
Figure 15. Ratio of temperature at $1/e^2$ radius to center temperature.

COMPUTED TEMPERATURES
FOR GAUSSIAN PROFILES

α_{PE} = 1485 α_{ch} = 166

α_{PE} = 250 α_{ch} = 250

α_{PE} = 250 α_{ch} = 250,
        32 μm Scatter

Wavelength : 514.5 nm
Exposure   : 10 s

$1/e^2$ Radius (μm)

1.0

0.5

0

100   200   300   400   500   600

Ratio of $1/e^2$ temperature to center temperature
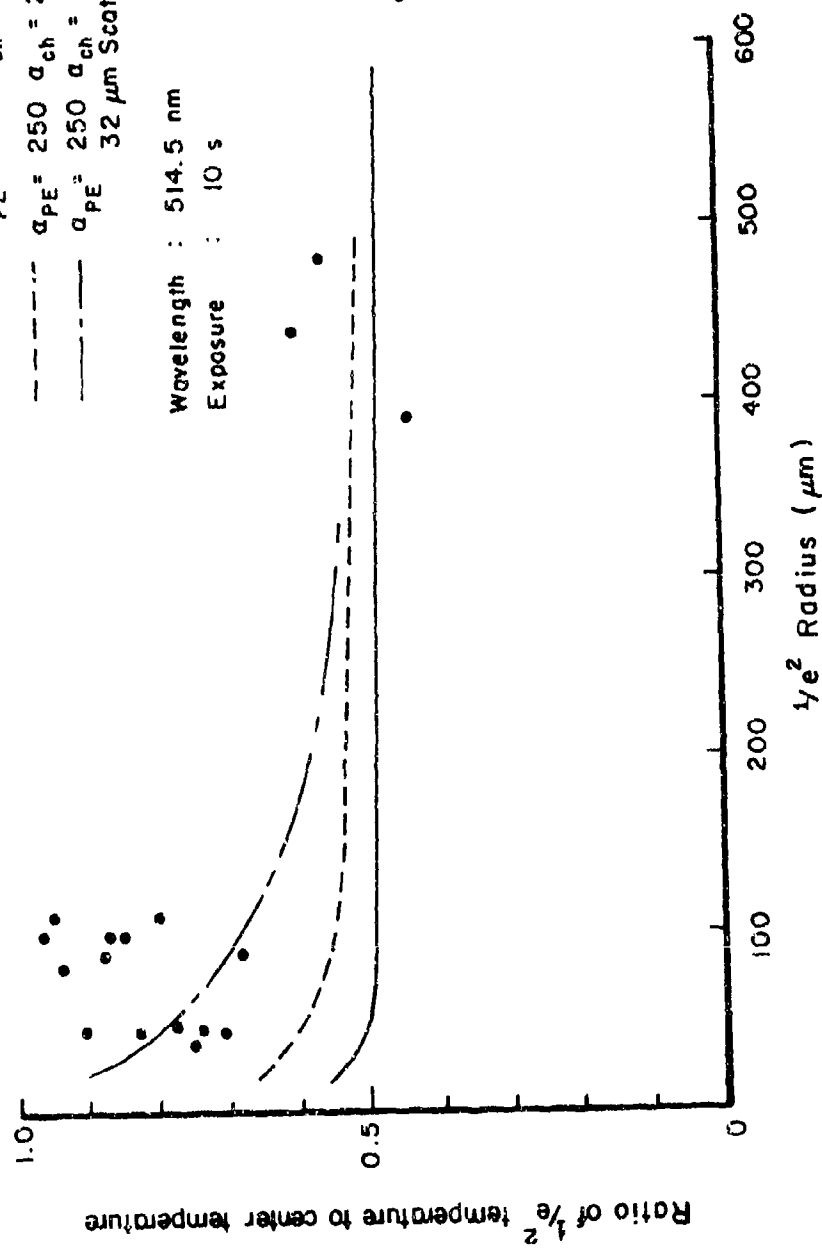
Figure 16. Ratio of temperature at $1/e^2$ radius to center temperature.
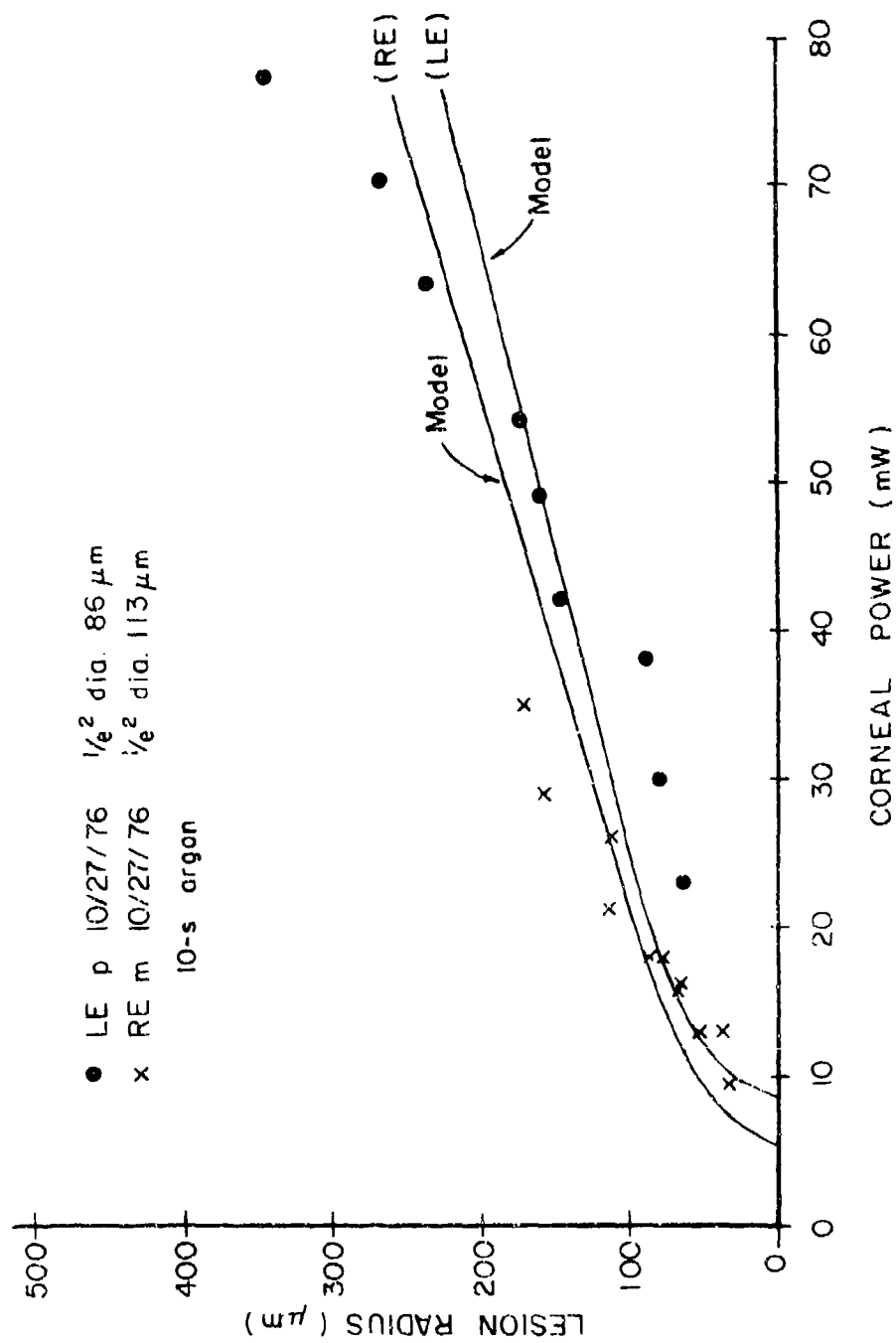
Figure 17. Lesion radius as a function of suprathreshold corneal power for 10-s argon irradiation. (LE-left eye, RE-right eye, p-paramacula, m-macula).

Comparisons of Model and Experimental Threshold Corneal Power

The threshold corneal power and resulting lesion radius for each experiment is tabulated in Tables A-6—A-8. Generally the lesion radii for argon irradiation were between 20 and 40 µm, with most values approximately 26 µm. The experimental threshold data for argon radiation is summarized in Table A-12. The table also includes the model-predicted corneal power to produce a 30-µm-radius lesion. Model and experimental threshold power as a function of image size is illustrated in Figure 18. Model data is represented by a solid line for the 30-ms exposure and a dashed line for the 10-s exposure. Model parameters of Table 3 are used in the calculation.

Due to Nd-Yag laser power limitations, thresholds could not be obtained for many of the 30-ms exposure conditions. For image radii between 70 and 115 µm, the average threshold power for 10-s irradiation was 26.2 mW (SD=9.4) for OVL threshold and 24.7 mW (SD=6.3) for MVL threshold. (Data from monkey 12/6/77 were omitted from the OVL average, and data from 5/13/77 were omitted from the MVL threshold.) The threshold lesion radii were 44-74 µm. The average power predicted by the IITRI model for a 40-µm-radius lesion was approximately 20 mW.
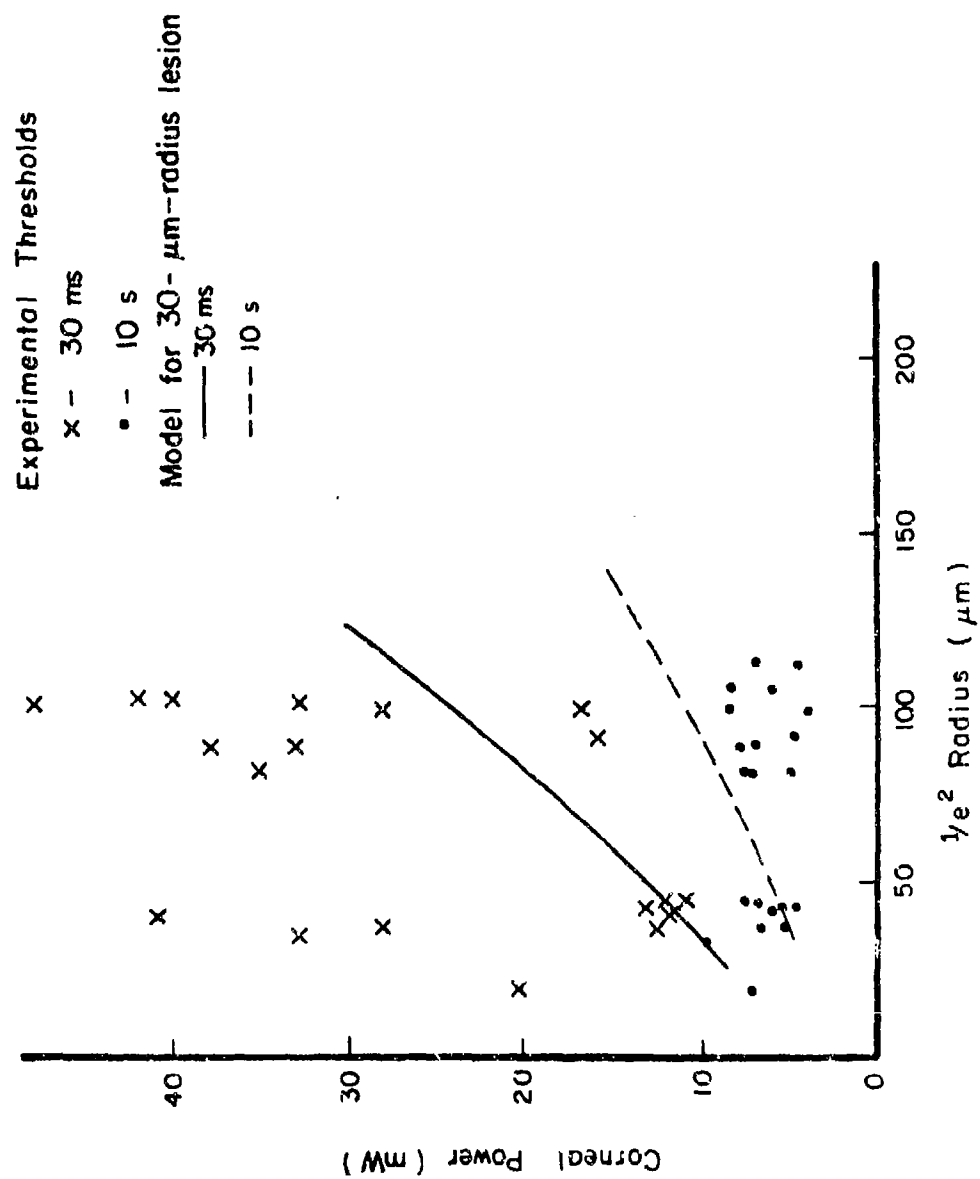
Figure 18.   Corneal power to produce 20- to 40-μm threshold lesions with argon (514.5 nm) irradiation.

DISCUSSION

Dye Cell

Measured and computed temperatures for the laser-irradiated dye cell were in general agreement. Although the values for a single experiment sometimes differed as much as 30%, average ratios of experimental temperature to model temperature were close to one.

The agreement of the dye cell data validates:

(a) The accuracy of the model in a uniform media of known thermal parameters.

(b) The ability of the microthermocouple to measure temperature (cf. "Measurement of Retinal Intensity Profile with Microsensors," Appendix B).

(c) The suitability of the experimental system for mapping temperature-time histories throughout a simple system.

Animal Results

The disagreement between model and experimental values illustrated in the Results section of this report requires a close examination of the experimental data. Either the model is very inaccurate or the experimental values are wrong. The invasive nature of the experiment may cause perturbations of the physical system which lead to inaccuracies in the experiment. Some errors which may affect the experimental results include: (1) probe measurement errors due to averaging of the temperature profile, (2) threshold measurements invalidated by significant eye-tissue alterations due to the extensive surgery required for the experiment, and (3) inaccurate profile measurements.

The model itself may also be in error due to factors not accounted for in the algorithm. Some factors that could affect the accuracy of the model solution include: (1) inaccurate perfusion rates, (2) scatter in the tissue which is not properly represented in the model, (3) inaccurate absorption parameters, and (4) the tissue not being a homogeneous, isotropic, well-ordered system as the model assumes. Estimates of the magnitude of these errors and their effect on the results will be discussed in the following paragraphs.

Comparison of Threshold Values with Values from th Literature

In Figure 19, the argon-irradiation threshold values obtained in this research are compared to values from the literature. Retinal energy density is plotted as a function of retinal image diameter $(1/e^2)$. Values reported by Beatrice and Frisch (1),
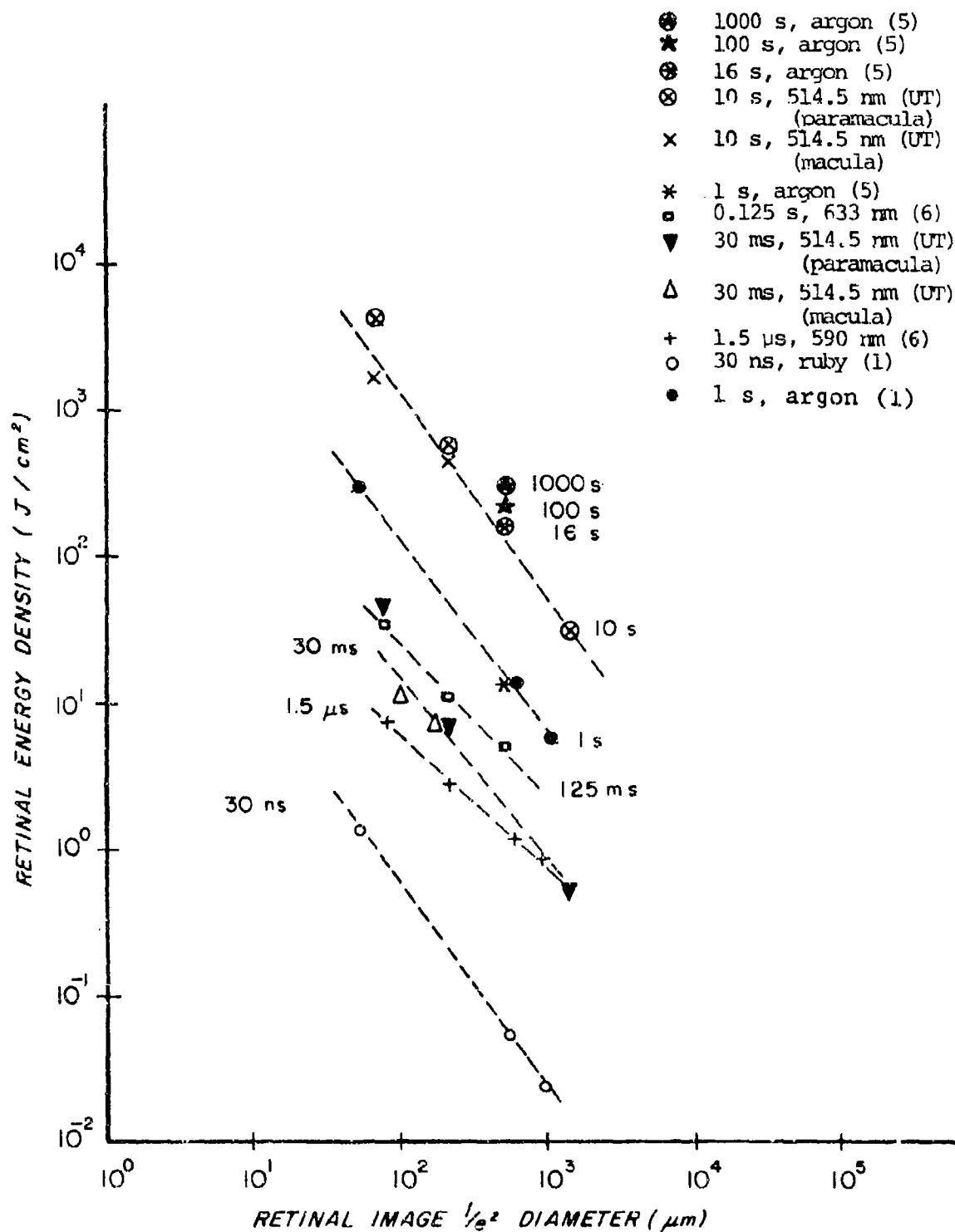
Figure 19. Threshold retinal density as a function of image size.
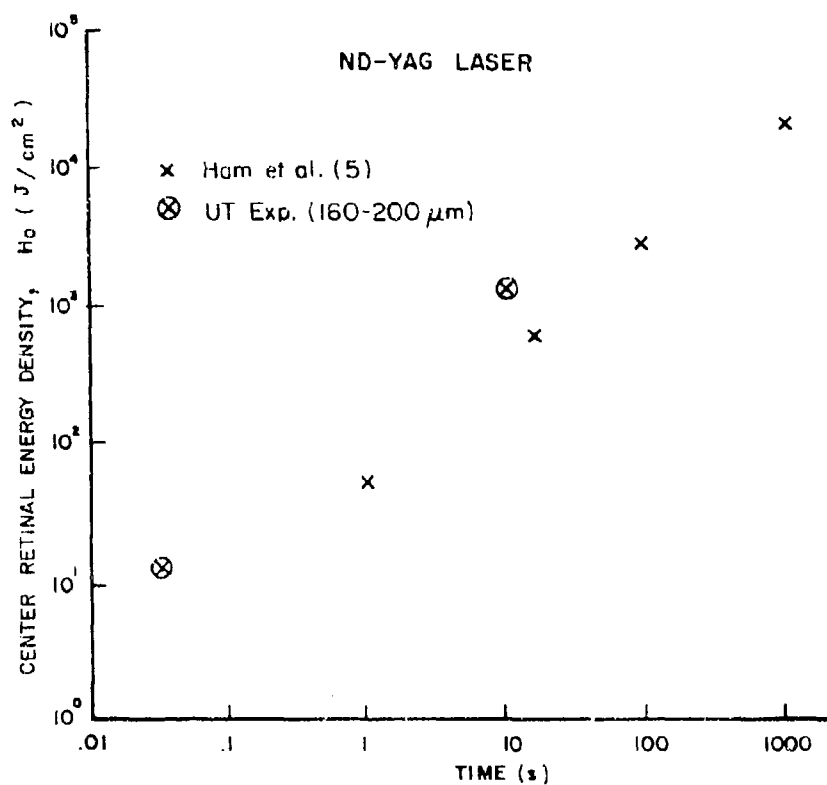
Figure 20.   Threshold retinal density as a function of radiation time.

Ham et al. (4,5), and Hillenkamp (6) are plotted for comparison on this figure. Our 10-s values agree very closely with the values from Ham et al. (5). The slope of the 30-ms and 10-s UT data agrees very well with the slope of the 1-s data of Beatrice and Frisch (1). From this figure it appears that our threshold values fit quite well with previously reported values from the literature.

In Figure 20, our neodymium threshold data are compared with the data of Ham et al. (5) for a 500-μm, $1/e^2$ image diameter. Their values of threshold energy density versus time of exposure compare well with our values for 160- to 200-μm-diameter beams.

Prediction of Temperature Rise

The effect of thermal parameters on predicting temperature with the IITRI model can be determined if the heat conduction equation is solved in terms of dimensionless variables. The heat-conduction equation with a Gaussian source term and perfusion sink is represented as:

$$\frac{\partial v}{\partial t} = \alpha\left(\frac{1}{r}\frac{\partial}{\partial r}(r\frac{\partial v}{\partial r}) + \frac{\partial^2 v}{\partial z^2}\right) + \frac{\beta H_o}{\rho c}(e^{-\frac{r^2}{2\sigma^2}}e^{-\beta z}) - Qv \qquad (4)$$

where
   $v(°C)$ = temperature rise
   $t(s)$ = time
   $\alpha(cm^2/s)$ = diffusivity
   $r(cm)$ = radial dimension
   $z(cm)$ = axial dimension
   $\beta(1/cm)$ = absorption coefficient
   $H_o(cal/cm^2\text{-}s)$ = center irradiance of source
   $\rho(g/cm^3)$ = density of tissue
   $c(cal/g\text{-}°C)$ = specific heat
   $\sigma(cm)$ = standard deviation of Gaussian source
   $Q(1/s)$ = convective heat loss due to perfusion (cm^3 blood
          flowing through cm^3 of tissue per second)

By introducing dimensionless variables for a medium with radiation absorption in one layer, the solution to equation 4 becomes independent of conductivity, specific heat, and irradiance. Dimensionless radial and axial parameters are automatically scaled to compensate for absorption coefficient and image size variations. Dimensionless temperature is achieved by substituting the following relations into equation 4.

   Let

   $\tau = t\alpha/\sigma^2$ (dimensionless time)   (5)

   $\xi = z\beta$ (dimensionless axial dimension)   (6)

   $\eta = r/\sigma$ (dimensionless radial dimension)   (7)

Equation 4 becomes

$$\frac{\partial v}{\partial \tau} \; \frac{\alpha}{\sigma^2} = \alpha \left(\frac{1}{\sigma^2} \; \frac{1}{\eta} \; \frac{\partial}{\partial \eta} \; (\eta \; \frac{\partial v}{\partial \eta}) + \beta^2 \; \frac{\partial^2 v}{\partial \xi} \right) \tag{8}$$

$$+ \; \frac{\beta H_0}{\rho c} \; e^{- \frac{(\eta^2 + \zeta)}{z}} - Q v$$

or

$$\frac{\partial v}{\partial \tau} = \frac{1}{\eta} \; \frac{\partial}{\partial \eta} \; (\eta \frac{\partial v}{\partial \eta}) + (\beta \sigma)^2 \; \frac{\partial v^2}{\partial \xi^2} + \frac{\beta \sigma^2 H_0}{\alpha \rho c} \; e^{-(\frac{\eta^2}{2} + \xi)} - \frac{Q \sigma^2 v}{\alpha} \tag{9}$$

Equation 9 has the dimension of temperature.

Now we let

$$\theta = \frac{v \rho c \alpha}{\beta \sigma^2 H_0} \qquad \text{(dimensionless temperature rise)} \tag{10}$$

and substitute for v in equation 9:

$$\frac{\partial \theta}{\partial \tau} = \frac{1}{\eta} \; \frac{\partial}{\partial \eta} \; (\eta \; \frac{\partial \theta}{\partial \eta}) + (\beta \sigma)^2 \; \frac{\partial^2 \theta}{\partial \xi^2} + e^{-(\frac{\eta^2}{2} + \zeta)} + \frac{Q \sigma^2 \theta}{\alpha} \tag{11}$$

Other relations commonly associated with the diffusion equation are the characteristic radial conduction time (i.e., time constant) R_{Tc}:

$$R_{Tc} = \frac{\sigma^2}{\alpha} \; (s) \tag{12}$$

and the axial time constant, A_{Tc}:

$$A_{Tc} = \frac{1}{\alpha \beta^2} \; (s) \tag{13}$$

If we assume a retinal image with a $1/c^2$ radius of 200 μm, diffusivity of 0.0015 cm²/s, and an absorption coefficient of 1000 cm⁻¹, the radial time constant is

$$R_{Tc} = \frac{(0.01 \text{ cm})^2}{1.5 \times 10^{-3} \text{ cm}^2/s} = 0.067 \, s$$

The axial time constant would be

$$A_{Tc} = \frac{1}{(1.5 \times 10^{-3} cm^2/s)\ (1000\ cm^{-1})^2} = 0.00067\ s$$

Conduction due to heating of the tissue is first in the axial direction and then in the radial direction for our example. The time constant for convective heat removal (i.e., blood perfusion) is approximately $1/Q$. Thus, for a high flow rate of 60 cm³ of blood per minute per 100 cm³ of tissue

$$Q = \frac{(60\ cm^3/min)}{(100\ cm^3)\ (60\ s/min)} = 0.01\ s^{-1}$$

or a time constant of 100 s. When the convective-heat-loss time constant is compared to radial and axial conduction time constants, it is apparent that perfusion does not affect the solution. The relative magnitudes of the source and sink terms is illustrated in equation 11. At $\eta=0$ and $\xi=0$ the source is equal to 1.0. The corresponding value of convective heat loss is

$\frac{Q\sigma^2}{\alpha}\ \theta$. For our example of $\alpha = .0015\ cm^2/s$, $\sigma=100\ \mu m$, and $Q=0.01$,

$$\frac{Q\sigma^2}{\alpha} = 6.7 \times 10^{-4}.$$

Since θ is generally much less than 1, the perfusion term does not influence the solution.

Determinations of θ were made by rewriting the UT model in terms of dimensionless variables. Calculations were performed for Gaussian profiles for several values of the parameter $\beta\sigma$. The calculated profiles show the effects of absorption parameter variation and image size variation. All calculations were completed for a single-layer absorber with homogeneous thermal properties.

In Figure 21, a plot of dimensionless temperature increase versus dimensionless time for Gaussian irradiance profiles is illustrated. Values of temperature rise for $\beta\sigma$ parameter values from 4×10^{-4} to 4×10^3 are plotted versus time at an axial position $\xi = .048$ corresponding to the first model grid point and radial position $\eta = 0$. For short-duration exposures, the temperature versus time asymptotically approaches the value $\tau e^{-\xi}$.
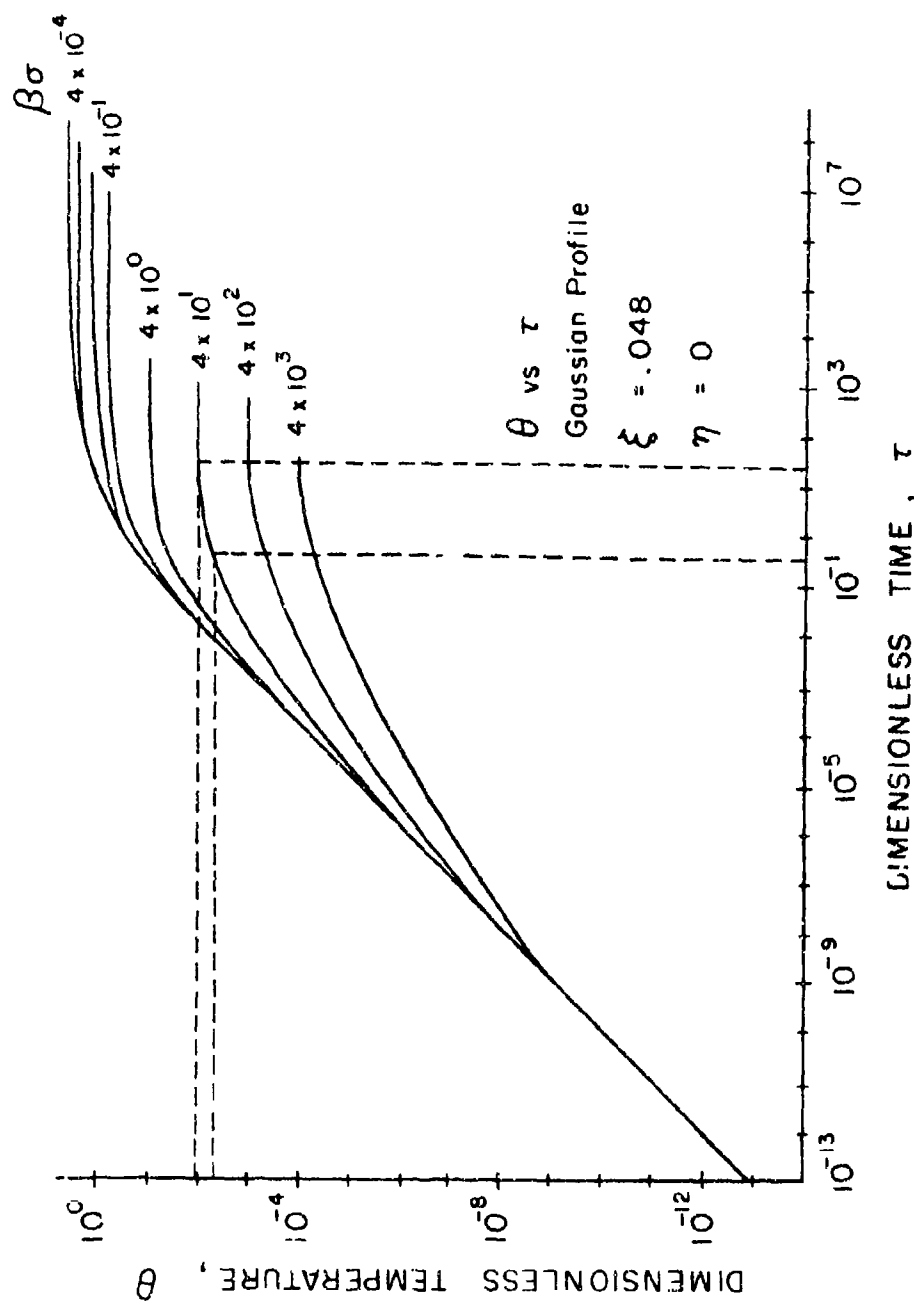
Figure 21. Dimensionless temperature versus dimensionless time for various values of the parameter $\beta\sigma$ for a Gaussian irradiance profile. For monkey eye of 200-μm 1/e^2 radius and β=4000 cm^{-1}, $\beta\sigma$ is 40. Corresponding τ for 30 ms and 10 s would be 0.45 and 15 respectively.

44

In the absence of conduction

$$\theta = e^{\frac{-\eta^2}{2}} \quad e^{-\xi} \tau \qquad \text{for } 0 \leq \eta < \sqrt{6} \quad \xi > 0 \tag{14}$$

$$\theta = 0 \qquad \qquad \text{for } \eta > \sqrt{6}$$

At longer time, the steady-state temperature is determined by the value of $\beta\sigma$. The ratio of steady-state temperatures is inversely proportional to the $\beta\sigma$ ratio.

In Figure 22, the effect of large $\beta\sigma$ ($\beta\sigma=40$) on axial conduction is illustrated. Dimensionless temperature versus dimensionless axial distance is plotted in the plane of the figure, while θ versus η is plotted in the isometric plane. For dimensionless time values less than .001, very little radial conduction has occurred; most of the conduction has been in the axial direction. For values of τ greater than .001, radial conduction begins to take place since the axial gradients are small.

As $\beta\sigma$ is increased, the primary term in equation 11 is
$(\beta\sigma)^2 \frac{\partial^2 \theta}{\partial \tau^2}$; so the shapes of the curves in Figure 22 do not change, but temperature scale and time values are shifted by the inverse ratio of $(\beta\sigma)^2$.

With the dimensionless model the radial and axial dimensions are automatically scaled to compensate for absorption parameter and image site variations. The effect of each parameter on the solution is readily determined since only simple multiplications are required to adjust the solution for new parameter values. This facilitates the identification of critical parameters.

Consider an absorption coefficient of $\beta = 4000$ cm^{-1} and image standard deviation of 0.01 cm. The dimensionless temperature response would be given by the $\beta\sigma=40$ curve of Figure 21. Real time would be obtained by multiplying the τ axis by

$\frac{\sigma^2}{\alpha}$ (i.e., $\frac{10^{-4}}{1.5\times10^{-3}} = 0.067$). Temperature rise in °C would be achieved by multiplying θ by $\frac{\beta\sigma^2 H_0}{\rho c \alpha}$ (i.e., $\frac{4000 \times 10^{-4} H_0}{1 \times 1 \times 1.5\times10^{-3}} = 60 H_0$).

Reduction of β to 400 cm^{-1} would change the transient response to the $\beta\sigma=4$ curve. The time scale would not change but temperature would be obtained by multiplying θ by $6H_0$. H_0 is related to retinal power by the relation

$$P_R = 2\pi H_0 \sigma^2 \quad \text{(cal/s)} \tag{15}$$
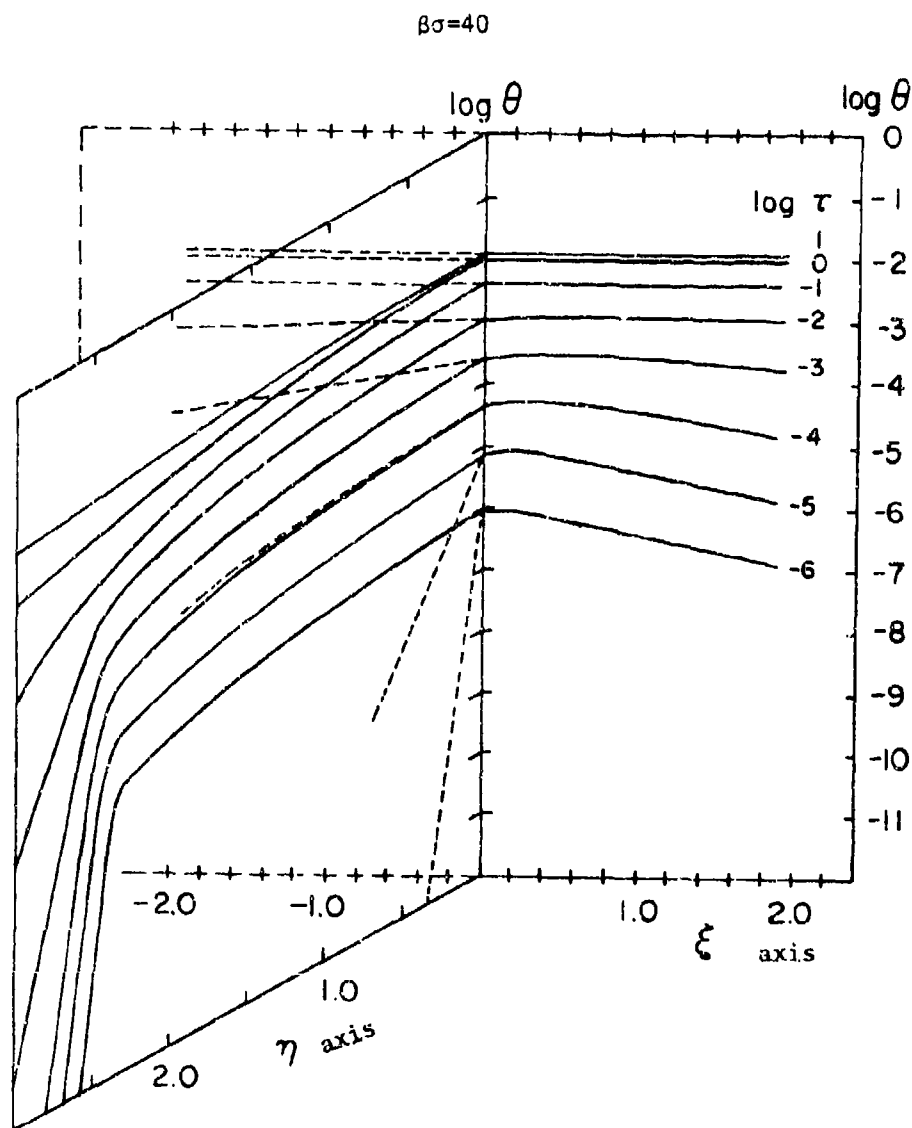
Figure 22. Isometric plot of log dimensionless temperature
(θ) versus dimensionless axial (ξ) and radial (η)
distances for various values of log dimensionless
time (τ).

or in terms of corneal power, CP,

$$CP = \frac{2\pi H_o o^2}{TOM} \text{ (cal/s)} \tag{16}$$

where TOM is the transmission of the ocular media.

Continuing with the above example, suppose CP = 10 mW (41.84 cal/s) and TOM = 0.85. Then H_o = 56.5 W/cm². For β = 4000 cm⁻¹, θ at 30 ms and 10 s would be roughly, from Figure 21, 6.83x10⁻³ and 1.08x10⁻² respectively. The temperature rise in °C would be 23.2°C at 30 ms and 36.6°C at 10 s.

Temperature Rise and Damage

The prediction of damage at a point in retinal tissue is based upon the empirically derived rate process o' equation 1 repeated here for reference:

$$\Omega(z,r) = C_1 \int_{t_i}^{t_f} \exp(-C_2/T(r,z))dt$$

The rate constants C_1 and C_2 are discussed in references 7, 8, 9, 10, and 11. Equation 1 is evaluated from the onset of the laser-induced temperature rise (t_i) to the final recovery of the temperature transient (t_f).

Generally, the damage which occurs at a point in tissue is a function of not only the peak temperature at the point, but also upon rise time and decay characteristics of temperature as a function of time. For short exposure durations, however, damage is only a function of the peak temperature at a point and its decay transient at the end of the short exposure. For long exposures, the temperature response approximates a step function for the duration of the exposure (the temperature decay can be neglected), and the damage equation reduces to

$$\Omega(z,r) = t_o C_1 \exp(-C_2/T(r,z)) \tag{17}$$

where t_o is the duration of the exposure in seconds. From equation 17 the steady-state temperature in °K at which Ω is unity may be determined:

$$T_{ss} = \frac{C_2}{\ln C_1 + \ln t_o} \tag{18}$$

According to equation 18, we would expect damage at every radial or axial point that exceeds a temperature of T_{ss} for a long-term exposure.

For argon radiation, measured maximum temperatures were generally lower than IITRI-model predictions ($\alpha_{PE} = 1485$ cm^{-1}) (Figs. 13 and 14). Also, the ratio of temperature at the $1/e^2$ radius to center temperature was much larger for the experimental data than for model values. Since the differences in maximum temperatures was a function of image size, we postulated the following sources of error:

(a) Incorrect measurement of image size
(b) Averaging of temperature by probe
(c) Movement of eye, so temperature scan would not pass through center of beam
(d) Incorrect model parameters such as absorption coefficient
(e) Scattering of light such that the standard deviation of the source term is larger than standard deviation of retinal image.

In previous work we estimated our error in the measurement of image size to be ± 10% (3, 9, 10, 11). However, reexamination of original data from this research indicated that much larger errors may have occurred in a few eyes. Recalculation of the $1/e^2$ paramacular image radius for monkey 10/27/76 yielded an estimate of 115 µm rather than 44 µm. The 43 µm paramacular image radius of monkey 2/9/77 could have been as large as 96 µm according to an original strip chart record. Also, the size of images less than 50 µm and larger than 200 µm tended to vary. Generally the tendency would be for an image to increase in size during an experiment. This type of error would shift an experimental point to the right in Figures 13, 14, and 20. In Figures 15 and 16 a point would be shifted to the right for the increased image size and down due to recalculation of the $1/e^2$ temperature at a distance farther from the center of the beam. With the exception of a few points we doubt that incorrect measurements in image size would account for the differences in Figures 15 and 16.

Temperature averaging by the probe would be significant only in regions of large axial and radial gradients. Based upon experimental data this error is estimated to be less than ± 1% at 30 ms and 10 s.

A problem that was not anticipated during the experiment was a slight movement of the eye. During an experiment a beam scan was made with the probe in the neural layer. Next, the probe was retracted into the absorbing layers and position was adjusted for maximum temperature rise. Next, a radial temperature scan was made for 30-ms irradiations. After the scan, laser tube current was lowered and a radial scan was taken for a 10-s irradiation. Slight movement of the laser beam with respect to the temperature probe would result in recording a "low" maximum temperature. A correction for this type of error would move the points of Figure 14 upward.

The critical experimental errors are associated with image size and measurement of maximum temperature. Model errors are generally associated with estimation of parameters. The value for the absorption coefficient of the pigment epithelium of 1485 cm^{-1} is much higher than estimates by the University (9,10) of approximately 360 cm^{-1}.

Until the development of the dimensionless model, we could not isolate the effect of errors in absorption coefficient from possible variation in other parameters. However, with this model and experimental temperatures and image size measurements, we could obtain two relations for an absorption coefficient, β. One relation was based upon equation 10. Solving for β and introducing a subscript 2,

$$\beta_2 = \frac{V\rho c\alpha}{\theta\sigma^2 H_0} = \frac{vk2\pi}{CP\theta TOM} \tag{19}$$

Average values of v and CP for 30-ms and 10-s exposures were taken from experiments that had approximately the same image size. The image standard deviations were averaged to obtain an average σ. Exposure times were converted to dimensionless time using equation 5.

In the dye cell experiments, for example, a 10-s exposure corresponded to a dimensionless time of 76. For 10-s experiments that had a standard deviation of approximately 125 μm, an average value of maximum temperature, v, and input power, CP, was computed. Data represented by Figure 21 was entered at $\tau=76$, and a value of θ was obtained for each $\beta\sigma$ curve. For each θ, equation 19 was used to compute a value of β_2.

A second estimate of absorption coefficient was obtained by the relation

$$\beta_1 = \frac{\beta\sigma}{\sigma} \tag{20}$$

where σ was the average standard deviation of the image (such as 125 μm) and $\beta\sigma$ values corresponded to curve values such as 0.4, 4, 40, etc. For each value of $\beta\sigma$, the paired values β_1, β_2 were plotted as a point. The curve for the dye cell for $\tau=76$ (10 s) is shown in Figure 23 along with the curve for $\tau=0.24$ (30 ms). The intersection of these curves with the $\beta_1=\beta_2$ line would indicate the value of β that best matches experimental and model temperatures. From Figure 23 we would expect the absorption coefficient of the dye cell to be 600 cm^{-1} or larger.

When the same technique was applied to 30-ms and 10-s argon data from the monkey eye, β appeared to be in the range of 100 to 250 cm^{-1}. However, for small images ($\sigma\approx20$ μm) the absorption coefficient appeared to be 70 cm^{-1} as shown in Figure 24. The estimate of $\beta=70$ from small-image data suggests tha the standard
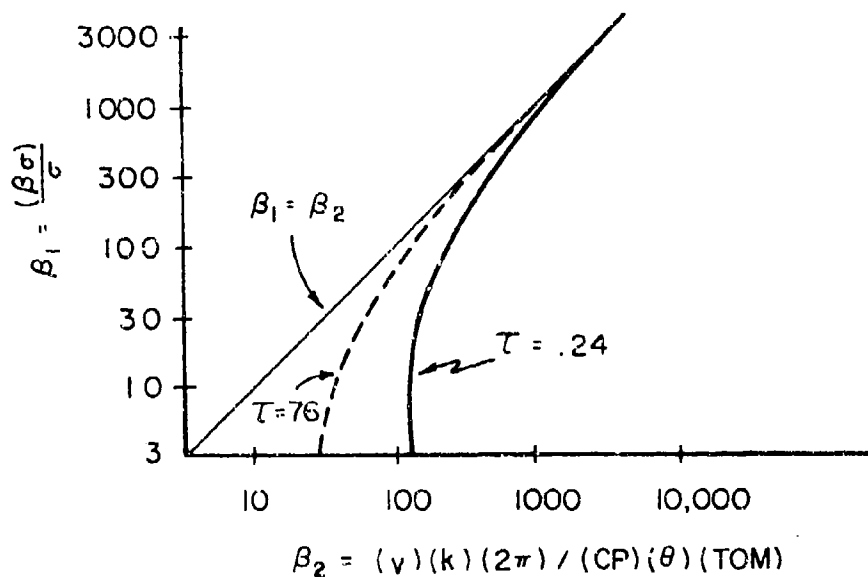
Figure 23. Determination of absorption coefficient β for argon irradiation of dye cell, using measured temperature and predicted dimensionless temperature. Image standard deviations averaged 125 μm, and irradiation times were 0.03 and 10 s.
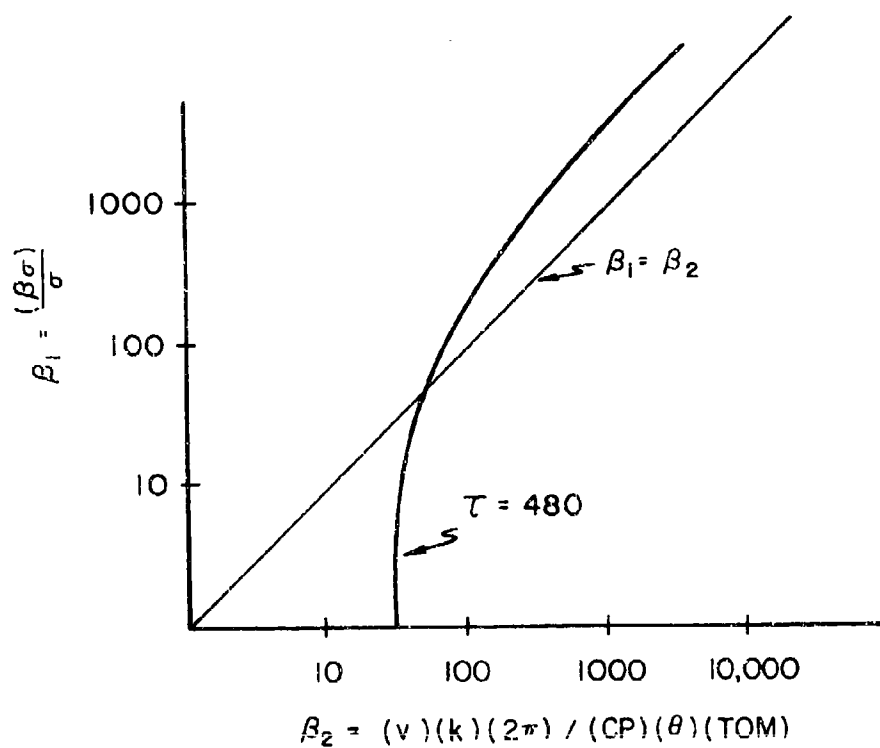
Figure 24. Determination of absorption coefficient β for argon irradiation of monkey eye, using measured and computed dimensionless temperatures. Image standard deviations averaged 20 μm, and irradiation time was 10 s.

deviation of the source term is larger than the value obtained from measurements of intensity profile made in front of the retina. The data of Figures 13 through 16 and 24 combine to support an argument for an absorption coefficient of approximately 250 cm^{-1} and scattering of light in the absorbing layers of the eye.

At the Nd-Yag wavelength, the absorption coefficient was estimated to be in the range 60 to 125 cm^{-1} for the monkey. This low value of absorption would suggest that conduction is primarily in the radial direction. Lowering the value in the model, however, would increase the difference between model and experimental data.

The ability of the IITRI model to predict damage is best discussed with the aid of Figure 18. The large scatter of the 30-ms experimental data is reduced when individual points are reexamined. All four of the x values that have a corneal power $\geq$ 20 mW and 1/e^2 radius < 50 μm are questionable. The 41- and 33-mW values are from right eyes for which we do not have left-eye data because of blanching. The 28 mW represents a left paramacular irradiation. Thresholds for a similar size image in the macula and thresholds for the macula and paramacula of the right eye were 23 ± 0.5 mW. The 20-mW threshold was from an eye that may have had an image nearer to 100 μm. The two low values (16 mW) of 30-ms threshold for 1/e^2 radius of 100 μm were from the same experiment. If these points are eliminated, two trends are seen. First, the threshold power for 10-s argon radiation is approximately constant over the range of experimental points. Second, threshold power as a function of image size for 30-ms irradiation increases at a faster rate than predicted by the IITRI model. The IITRI model appears to be optimized for small-image data. Optimization appears to be associated with the rate coefficients C_1 and C_2 of equation 1. This is illustrated in Figure 25 where the maximum temperature rise for 10-s argon radiation is plotted as a function of image size. The rather constant experimental temperature would be expected when the temperature response has time to reach a steady-state value. Basically, the model is overestimating temperature for small images and compensating for the error in the selection of values for C_1 and C_2.
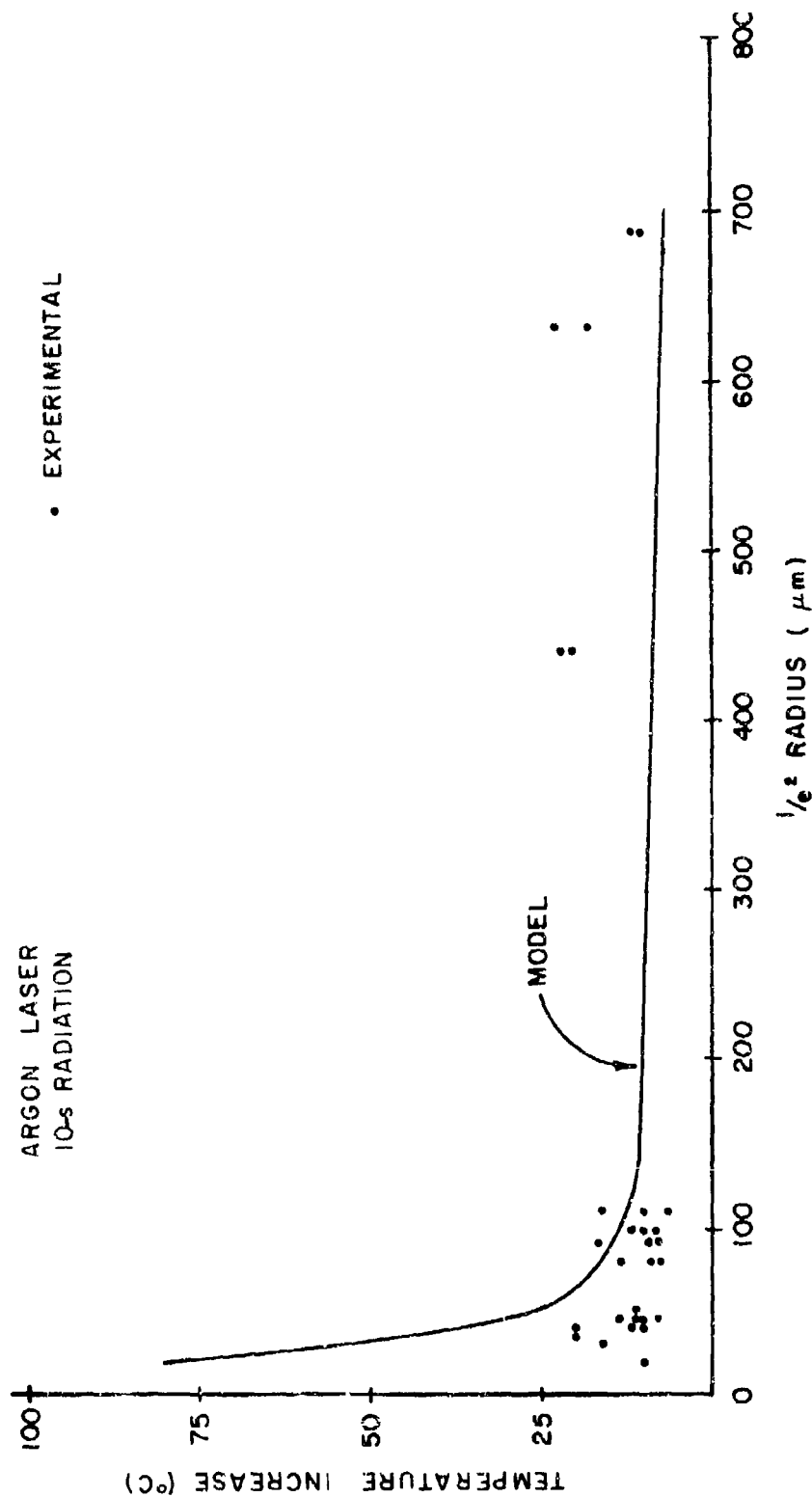
Figure 25. Temperature increase in PE at center of beam at the end of 10^{-s}
threshold irradiation. The solid curve represents the average model
predicted temperature increase.

CONCLUSIONS

The dye cell experiment validates the accuracy of the experimental procedure and the temperature model in a simple system with known thermal parameters.

In the monkey eye, measured temperatures do not agree with model values for small ($1/e^2$ radius < 50 µm) and large ($1/e^2$ radius > 200 µm) images. Also, measured temperatures at the $1/e^2$ radius of the image are always higher than model values. Two factors believed to contribute to this difference are (1) model absorption coefficient is too high and (2) scattering broadens the source term in the tissue. These factors, however, do not fully explain the difference between measured and computed temperature profiles.

The IITRI model correctly predicts damage over a wide range of argon and Nd-Yag irradiation times and image sizes; however, damage is not predicted for threshold irradiations for large images. Rate coefficients for the IITRI model seem to have been selected so that the combined temperature-rate process model would correctly predict damage for data appearing in the open literature.

When the two models are examined independently, evidently the following changes for the IITRI model should be considered to optimize results.

1. The absorption coefficient of the PE is too high. A value in the range of 250 cm^{-1} would produce closer agreement between measured and predicted temperatures.

2. Scattering should be considered in computing the source term in the prediction of temperature rise due to minimal images. This could be accomplished in the IITRI model by overestimating the size of the image.

3. Rate process coefficients should be modified to reflect the occurrence of damage for steady-state temperature increases below 20°C. Coefficients should be obtained from a plot of ln (exposure time) versus 1/threshold temperature.

4. The blood-flow section of the model should be omitted.

5. The number of grid points in the model should be expanded to increase the accuracy near the $1/e^2$ radius where the source term is truncated.

6. A dimensionless solution to the heat-conduction equation should be considered to avoid scaling and parameter value errors.

REFERENCES

1. Beatrice, E. S., and G. D. Frisch. Retinal laser damage thresholds as a function of image diameter. Arch Environ Health 27:322-326 (1973).

2. Cain, C. P., and A. J. Welch. Thin film temperature sensors for biological measurements. IEEE Trans Biomed Eng 21(4): 421-423 (1974).

3. Forster, L. D., et al. Combination sensors for the measurement of light distribution, temperature increase and electrical activity in the retina. Biomed Sci Instrum 13: 75-81 (1977).

4. Ham, W. T., et al. Effects of laser radiation on the mammalian eye. Trans NY Acad Sci 28(4):517-526 (1966).

5. Ham, W. T., et al. Retinal sensitivity to damage from short wavelength light. Nature 260(5547):153-155 (1976).

6. Hillenkamp, F. Univ of Frankfurt, Frankfurt, Germany, personal communication, June 1976.

7. Priebe, L. A., and A. J. Welch. Asymptotic rate process calculations of thermal injury to the retina following laser irradiation. J Biomed Eng 100:49-54 (1978).

8. Takata, A. N., et al. Thermal model of laser-induced eye damage. Final report for USAF School of Aerospace Medicine, Brooks AFB TX, contract F41609-74-C-0005, IIT Research Institute, Chicago IL, 1974.

9. Welch, A. J., et al. Temperature rise in fundus exposed to laser radiation. Final report for USAF School of Aerospace Medicine, Brooks AFB TX, contract F41609-73-C-0031, University of Texas, Austin TX, 1974.

10. Welch, A. J., et al. Model of thermal injury based on temperature rise in fundus exposed to laser radiation. Final report for USAF School of Aerospace Medicine, Brooks AFB TX, contract F41609-74-C-0025, University of Texas, Austin TX, 1975.

11. Welch, A. J., et al. Limits of applicability of thermal models of thermal injury. Final report for USAF School of Aerospace Medicine, Brooks AFB TX, contract F41609-76-C-0005, University of Texas, Austin TX, 1976.

TABLE A-1. EXPERIMENTAL CONDITIONS FOR DYE CELL

Wavelength = 514.5 nm, Dye Cell Transmittance*= 0.931

$1/e^2$ power radius (μm)	Average absorption (cm^{-1})	Exposure power in mW 30 ms	Exposure power in mW 10 s	Probe diameter (μm)	Probe sensitivity (μV/°C)
43.57	679.1	2.29	2.29	30	22.20
74.00	697.0	4.25	4.25	22	20.00
74.00	398.8	4.40	4.40	25	19.61
98.81	724.6	7.77	7.77	22	20.00
99.98	398.8	13.31	7.21	25	18.61
103.80	685.4	14.42	-	30	22.20
109.30	630.8	9.24	-	30	22.20
116.20	398.8	6.73	6.73	25	18.61
122.03	398.8	29.95	7.40	25	18.61
126.50	772.5	7.00	7.00	30	22.20
148.80	617.9	13.13	13.13	25	18.61
150.35	680.7	4.07	4.03	30	22.20
172.50	556.0	13.98	-	30	22.20
201.50	398.8	44.38	-	25	18.61
316.15	617.9	12.76	12.76	25	18.61
430.90	680.7	48.07	24.04	30	22.20
458.80	694.4	67.30	21.86	30	22.20
472.44	396.8	78.40	36.98	25	18.61
530.46	779.5	107.00	22.00	30	22.20
720.75	664.3	133.13	44.38	22	20.00

Wavelength = 1060 nm, Dye Cell Transmittance*= 0.570

$1/e^2$ power radius (μm)	Average absorption (cm^{-1})	Exposure Power in mW 30 ms	Probe diameter (μm)	Probe sensitivity (μV/°C)
53.94	457.4	11.20	25	18.61
91.40	386.6	16.90	25	18.61
407.34	442.3	92.71	25	18.61
461.30	306.9	32.50	25	18.61
514.60	516.7	175.00	14	18.67
571.95	516.7	176.04	14	18.67
725.40	454.9	295.83	25	18.61
736.20	516.7	126.04	14	18.67
775.00	516.7	176.04	14	18.67
898.20	516.7	200.52	14	18.67

* Fraction of light at surface of dye cell that reaches the pigmented layer.

TABLE A-2. MAXIMUM EXPERIMENTAL AND MODEL TEMPERATURES FOR DYE CELL (λ = 514.5 nm)

Temperature at end of 30-ms irradiation

$1/e^2$ power radius (μm)	$\frac{1}{2}$ power radius (μm)	Average absorption (cm^{-1})	Exposure power (mW)	Probe depth (μm)	Temperature at Center of image (°C)		Temperature at $\frac{1}{2}$ power radius (°C)	
					Model	Experiment	Model	Experiment
43.5	26.6	679.1	2.2	HotSpot	9.8	12.1	6.9	7.6
43.5	26.6	679.1	2.2	-13.0	8.4	10.7	6.3	5.5
74.0	45.3	697.0	4.2	HotSpot	9.8	12.0	6.5	8.3
74.4	42.5	398.8	4.4	HotSpot	9.1	13.0	3.5	7.9
98.8	56.1	724.6	7.7	HotSpot	13.9	15.7	9.2	11.0
98.8	56.1	724.6	7.7	-22.2	10.5	10.2	6.9	7.8
98.8	56.1	724.6	7.7	-44.5	7.5	5.5	5.1	5.1
99.9	62.0	398.8	13.3	HotSpot	19.7	14.7	12.6	9.7
103.8	49.6	685.4	14.4	HotSpot	22.9	23.8	16.1	18.9
103.8	49.6	685.4	14.4	-29.7	13.5	12.6	10.7	10.5
103.8	49.6	685.4	14.4	-81.7	5.4	6.6	4.5	5.6
109.3	62.7	630.8	9.2	HotSpot	13.7	11.7	8.9	8.3
116.2	69.7	398.8	6.7	HotSpot	8.3	9.8	5.3	6.0
122.0	66.0	398.8	29.9	HotSpot	36.0	20.9	23.6	15.1
126.5	73.4	772.5	7.0	HotSpot	9.4	11.7	5.8	7.2
126.5	73.4	772.5	7.0	-59.5	3.7	4.5	2.5	3.3
126.5	73.4	772.5	7.0	-89.2	1.8	2.7	1.2	2.3
148.8	99.2	617.9	13.1	HotSpot	12.3	9.7	6.9	5.4
150.3	94.5	680.7	4.0	HotSpot	3.9	6.5	2.3	2.4
150.3	94.5	680.7	4.0	-89.1	0.9	2.7	0.5	1.7
172.5	90.8	555.6	13.9	HotSpot	10.8	13.4	6.8	8.5
201.5	114.7	398.8	44.3	HotSpot	24.1	12.2	14.7	6.9
316.1	174.3	617.9	12.7	HotSpot	3.9	2.6	2.2	1.5
430.9	257.3	680.7	48.0	HotSpot	7.8	5.4	4.1	2.8
430.9	257.3	680.7	48.0	-118.8	1.4	3.7	0.7	1.8
458.8	232.5	694.4	47.7	HotSpot	7.2	8.5	4.0	5.0
458.8	232.5	694.4	67.3	HotSpot	10.1	9.2	5.6	5.7
458.8	232.5	694.4	67.3	-37.1	7.1	8.5	3.5	5.2
458.8	232.5	694.4	67.3	-81.7	3.2	6.2	1.9	4.1
472.4	302.2	398.8	78.4	HotSpot	9.5	9.2	4.9	4.0
530.4	274.4	779.5	107.0	HotSpot	14.7	18.5	7.2	9.5
530.4	274.4	779.5	107.0	-59.4	7.1	12.3	3.5	6.4
530.4	274.4	779.5	107.0	-118.8	1.6	4.8	1.3	2.8
720.7	348.7	664.3	133.1	HotSpot	9.0	8.3	4.8	4.1
720.7	348.7	664.3	133.1	-89.1	2.4	1.5	1.3	1.1

Temperature at end of 10-s irradiation

$1/e^2$ Power radius (μm)	$\frac{1}{2}$ Power radius (μm)	Average absorption (cm^{-1})	Exposure power (mW)	Proba depth (μm)	Temperature at center of image (°C)		Temperature at $\frac{1}{2}$ power radius (°C)	
					Model	Experiment	Model	Experiment
43.5	26.6	679.0	2.2	HotSpot	11.8	14.4	8.9	10.2
43.5	26.6	679.0	2.2	-13.02	10.4	11.7	8.3	7.8
74.0	45.3	697.0	4.2	HotSpot	13.5	15.5	9.9	12.0
74.4	42.5	398.0	4.4	HotSpot	12.9	14.5	6.9	11.5
98.8	56.1	724.6	7.7	HotSpot	20.5	23.8	15.4	19.5
98.0	56.1	724.6	7.7	-22.2	17.4	18.4	13.4	15.2
98.8	56.1	724.6	7.7	-44.5	13.7	12.0	11.1	9.1
99.9	62.0	398.8	7.2	HotSpot	16.7	13.9	12.5	12.2
116.2	69.7	398.8	6.7	HotSpot	13.9	16.1	10.5	12.5
122.0	66.0	398.8	7.4	HotSpot	14.9	11.2	11.4	9.8
126.5	73.4	772.5	7.0	HotSpot	15.0	19.4	11.0	14.6
126.5	73.4	772.5	7.0	-59.5	9.0	11.4	7.4	9.9
126.5	73.4	772.5	7.0	-89.2	6.8	8.6	5.9	7.5
148.8	99.2	617.9	13.1	HotSpot	22.6	13.9	16.0	12.1
150.3	94.5	680.7	4.0	HotSpot	7.1	7.7	5.1	5.6
150.3	94.5	680.7	4.0	-89.1	3.7	6.3	3.1	4.9
316.1	174.3	617.9	12.7	HotSpot	11.3	8.1	8.3	6.5
130.9	257.3	680.7	24.0	HotSpot	14.9	4.7	10.5	3.6
430.9	257.3	680.7	24.0	-118.8	16.3	3.8	7.9	2.9
458.8	232.5	694.4	21.8	HotSpot	12.6	13.8	9.5	11.3
458.8	232.5	694.4	21.8	-29.7	11.7	11.7	9.0	9.5
458.8	232.5	694.4	21.8	-59.4	10.6	8.5	8.3	4.9
472.4	302.2	398.8	36.9	HotSpot	20.3	14.5	14.0	10.9
530.4	274.4	779.5	22.0	HotSpot	12.1	25.5	8.5	10.8
530.4	274.4	779.5	22.0	-59.4	10.2	21.3	7.6	9.6
530.4	274.4	779.5	22.0	-118.8	8.4	13.8	6.5	8.0
720.7	348.7	664.3	44.3	HotSpot	16.1	14.5	11.9	11.2
720.7	348.7	664.3	44.3	HotSpot	16.1	13.5	11.9	10.7
720.7	348.7	664.3	44.3	-89.1	13.1	9.0	10.3	7.3

TABLE A-3. MAXIMUM EXPERIMENTAL AND MODEL TEMPERATURES FOR DYE CELLS (λ= 1060 nm)

Temperature at end of 30-ms irradiation

$1/e^2$ Power radius (μm)	1/2 Power radius (μm)	Average absorption (cm^{-1})	Exposure power (mW)	Probe depth (μm)	Temperature at center of image (°C)		Temperature at 1/2 power radius (°C)	
					Model	Experiment	Model	Experiment
53.9	35.7	457.4	11.2	HotSpot	21.7	11.0	14.7	7.7
53.9	35.7	457.4	11.2	-89.1	4.0	4.2	3.3	3.6
88.6	54.9	384.3	17.0	HotSpot	18.2	12.0	11.9	7.5
88.6	54.9	384.3	17.0	-29.7	14.1	6.9	9.5	4.3
91.4	53.8	386.6	16.9	HotSpot	17.7	11.6	11.9	8.1
91.4	53.8	386.6	16.9	-77.2	5.8	7.9	4.3	5.8
91.4	53.8	386.6	16.9	-163.4	0.8	3.9	0.6	2.9
407.3	238.8	442.3	92.7	HotSpot	9.6	10.0	5.2	5.3
407.3	238.8	442.3	92.7	-187.2	0.4	4.3	0.2	2.5
461.9	306.9	370.0	32.5	HotSpot	2.4	2.9	1.3	1.4
514.6	266.6	516.7	175.0	HotSpot	13.2	12.0	7.0	6.8
571.9	330.1	516.7	176.0	HotSpot	9.9	9.2	5.1	4.7
725.4	325.5	454.9	295.8	HotSpot	11.8	13.1	6.3	7.3
725.4	325.5	454.9	295.8	-99.5	3.4	5.9	1.9	3.7
736.2	348.7	516.7	126.0	HotSpot	5.4	4.2	2.9	2.4
775.0	375.8	516.7	176.0	HotSpot	7.2	6.4	3.7	3.0
928.2	509.9	516.7	200.5	HotSpot	5.1	4.0	2.7	2.4

TABLE A-4. TEMPERATURE AT HALF-POWER RADIUS FOR HOT-SPOT
TEMPERATURE NORMALIZED TO 1°C

λ = 514.5 nm, 30-ms radiation, dye cell data

$1/e^2$ power radius (μm)	$\frac{1}{2}$ power radius (μm)	Model temperature (°C)	Experimental temperature (°C)	Difference (%)
43.57	26.66	0.711	0.630	-11.42
74.00	45.34	0.668	0.696	4.19
74.40	42.53	0.384	0.612	59.38
98.81	56.11	0.659	0.704	6.83
99.98	62.00	0.642	0.665	3.58
103.80	49.60	0.705	0.793	12.48
109.30	62.78	0.652	0.711	9.05
116.20	69.70	0.639	0.612	-4.23
122.03	66.02	0.654	0.721	10.25
126.50	73.43	0.619	0.622	0.48
148.80	99.20	0.566	0.552	-2.47
150.35	94.55	0.577	0.378	-34.49
172.50	90.80	0.628	0.638	1.59
201.50	114.70	0.609	0.564	-7.39
316.15	174.33	0.577	0.581	0.69
430.90	257.30	0.525	0.528	0.57
458.80	232.50	0.560	0.592	5.71
458.80	232.50	0.560	0.622	11.07
472.44	302.25	0.517	0.442	-14.51
530.46	274.40	0.490	0.516	5.31
720.75	348.75	0.534	0.493	-7.68

TABLE A-4.   TEMPERATURE AT HALF-POWER RADIUS FOR HOT-SPOT
TEMPERATURE NORMALIZED TO 1°C (continued)

$\lambda = 514.5$ nm, 10-s radiation, dye cell data

$1/e^2$ power radius (μm)	$\frac{1}{2}$ power radius (μm)	Model temperature (°C)	Experimental temperature (°C)	Difference (%)
43.57	26.66	0.757	0.711	-6.08
74.00	45.34	0.739	0.774	4.74
74.40	42.53	0.539	0.796	47.68
98.81	56.11	0.752	0.821	9.18
99.98	62.00	0.751	0.877	16.78
116.20	69.70	0.756	0.777	2.78
122.03	66.02	0.770	0.872	13.25
148.80	99.20	0.710	0.869	22.40
126.50	73.43	0.733	0.755	3.00
150.35	94.55	0.717	0.731	1.95
316.15	174.33	0.739	0.807	9.20
430.90	257.30	0.707	0.774	9.48
458.80	232.50	0.754	0.817	8.36
472.44	302.25	0.690	0.756	9.57
530.46	274.40	0.702	0.423	-39.74
720.75	348.75	0.744	0.776	4.30
720.75	348.75	0.744	0.796	6.99

TABLE A-4. TEMPERATURE AT HALF-POWER RADIUS FOR HOT-SPOT
TEMPERATURE NORMALIZED TO 1°C   (continued)

λ = 1060 nm, 30-ms radiation, dye dell data

$1/e^2$ power radius (μm)	$\frac{1}{2}$ power radius (μm)	Model temperature (^{o}C)	Experimental temperature (^{o}C)	Difference (%)
53.94	35.71	0.675	0.707	4.74
88.61	54.98	0.654	0.622	-4.89
91.40	53.89	0.672	0.696	3.57
407.34	238.82	0.539	0.530	-1.67
461.90	306.90	0.532	0.514	-3.38
514.60	266.60	0.536	0.569	6.16
571.95	330.15	0.516	0.519	0.58
725.40	325.50	0.540	0.558	3.33
736.20	348.70	0.554	0.589	6.32
775.00	375.88	0.519	0.474	-8.67
998.20	509.90	0.541	0.598	10.54

TABLE A-5. AXIAL TEMPERATURE FOR HOT-SPOT TEMPERATURE NORMALIZED TO 1°C

$1/e^2$ Power radius (μm)	Probe depth (μm)	Model temperature (°C)	Experimental temperature (°C)	Difference (%)
λ = 514.5-nm, 30-ms radiation, dye cell data				
43.57	-13.02	0.8582	0.8816	2.73
98.81	-22.29	0.7516	0.6497	-13.56
98.81	-44.58	0.5369	0.3503	-34.76
103.80	-29.72	0.5909	0.5283	-10.59
103.80	-81.73	0.2370	0.2794	17.89
126.50	-59.50	0.3915	0.3920	0.13
126.50	-89.20	0.1905	0.2366	24.20
150.35	-89.16	0.2281	0.4273	87.33
430.90	-118.88	0.1860	0.6801	265.65
458.80	-37.15	0.7054	0.9264	31.33
458.80	-81.73	0.3232	0.6732	108.29
530.46	-59.44	0.4844	0.6627	36.81
530.46	-118.88	0.1102	0.2624	138.11
720.75	-89.16	0.2719	0.2807	3.24
43.57	-13.02	0.8824	0.8126	-7.91
98.81	-22.29	0.8512	0.7731	-9.18
98.81	-44.58	0.6722	0.5063	-24.68
126.50	-59.50	0.5964	0.5918	-0.77
126.50	-89.20	0.4506	0.4433	-1.62
λ = 514.5-nm, 30-ms radiation, dye cell data				
150.35	-89.16	0.5246	0.8195	56.21
430.90	-118.88	0.6880	0.8097	17.69
458.80	-29.72	0.9320	0.8443	-9.41
458.80	-59.44	0.8387	0.6172	-26.41
530.46	-59.44	0.8430	0.8346	-1.00
530.46	-118.88	0.6942	0.5407	-22.11
720.75	-89.16	0.8174	0.6667	-18.44
λ = 1060-nm, 30-ms radiation dye cell data				
53.94	-89.16	0.1878	0.3829	103.91
88.61	-29.70	0.7723	0.5782	-25.13
91.40	-77.27	0.3320	0.6801	104.85
91.40	-163.46	0.0452	0.3345	640.05
407.34	-187.24	0.0508	0.4320	750.39
725.40	-99.56	0.2941	0.4508	53.28

Monkey	Image radius @ 1/e² point (μm)	Site	Eye	Corneal power (mW) OVL threshold	MVL threshold	Temperature of lesion center (°C) Model*	Using MVL power	Lesion radius (μm) for MVL threshold Model	Experiment
10/13/76	630	P	L	196	147	12.2	19.1	N.D.	65
	630	P	R	213.5	175	14.6	22.8	N.D.	104
10/22/76	440	P	R	143.5	129.5	20.5	35.1	N.D.	30
	440	P	L	210	141.8	22.5	48.3	N.D.	25
11/3/76	108	M	L	73.5	52.5	73.7	35.2	78.1	60
	99	P	L	56	28	39.6	25.8	37.2	25
11/8/76	101	M	L	32.9	16.8	25.0	30.2	N.D.	25
	93	P	L	31.2	15.8	29.5	36.3	<20	35
1/6/77	112	M	L	43.8	40.3	52.1	39.5	52	39
	88	P	L	32.3	32.9	54.0	28.9	55.0	20
	112	M	R	35.0	42.0	54.2	41.2	65	26
	88	P	R	38.5	38.5	63.2	35.4	66.0	39
1/19/77	82	M	L	56.8	44	87.2	52.8	76.6 (OVL)	40
	101	P	L	72.5	40.3	67.2	68.5	65	25
	82	M	R	---	35.0	69.4	74.2	62	25
	101	P	R	37.8	33.3	46.4	56.6	45	12.5
10/27/76	43	P	L	---	73.5	115.2	---	83	20
	43	P	R	101.5	77.0	121.0	---	84.1	20
1/26/77	36	P	R	35.6	33.0	163.2	---	56.3	20
2/9/77	43	P	R	---	41.3	66.8	---	39.3	20
2/23/77	45	M	L	22.2	13.3	57.6	20.3	34	20
	38	P	L	---	28	182	47.6	52.4	20
	45	M	R	16.8	12.6	31.1	19.3	35	20
	38	P	R	21.7	12.6	82	21.4	30	20
3/30/77	50	P	L	35	---	153	---	58	---
	67	M	R	23.8	---	67.9	---	46.8	---
	50	P	R	31.5	---	137.3	---	55.5	---
4/13/77	45	P	L	42.0	42.0	224.2	56.3	67.85	78.0
4/22/77	46	P	L	---	11.9	35.6	17.9	32.1	30
	44	M	L	---	10.9	55.0	17.5	33.4	35
	46	P	R	---	23.8	111.3	35.7	49.4	60
2/2/77	22	P	R	23.1	20.3	206.3	---	35	12.5
4/6/77	22	P	L	9.1	---	88.5	---	26.2	---

N.D. - No damage
P - Paramacula
M - Macula
L - Left eye
R - Right eye
* - Based on MVL threshold power. If MVL power was not available, then OVL threshold power was used.
MVL - Microscopically visible lesion
OVL - Ophthalmoscopically visible lesion
   Experimental threshold temperatures computed with equation 3.

TABLE A-7. THRESHOLD POWER, TEMPERATURE, AND LESION RADIUS FOR 10-s 514.5-nm ARGON LASER EXPOSURE

Monkey	Image radius @ $1/e^2$ point (µm)	Site	Eye	Corneal power (mW)		Temperature of lesion center (°C)			Lesion radius (µm) for MVL threshold	
				OVL threshold	MVL threshold	Model*	Using MVL power	Using OVL power	Model	Experiment
10/13/76	630	P	L	31.5	24.2	7.2	9.2	13.5	N.D.	52
	630	P	R	38.5	31.5	13.5	12.0	29.1	N.D.	88
10/22/76	440	P	L	20.3	15.8	7.1	16.7	17.6	N.D.	104
	440	P	R	27.3	19.8	8.9	21	30.9	N.D.	32.5
9/20/77	480	P	L	22	---	5.2	---	9.8	N.D.	---
	480	P	R	25	---	5.9	---	11.1	N.D.	---
11/3/76	108	M	L	12.8	6.3	12.9	6.0	13.5	N.D.	26
	98	P	L	14	8.8	18.1	12.3	19.3	<10	30
11/8/77	101	M	L	10.7	4.03	8.1	8.9	21.7	N.D.	26
	92	P	L	9	4.6	11.2	15 2	33.1	N.D.	40
1/6/77	112	M	L	7	7	12.1	15.0	15.5	N.D.	26
	87	P	L	8.1	7.4	16.3	8.9	9.4	N.D.	26
	112	M	R	8.4	4.6	7.8	8.9	18.6	N.D.	26
	87	P	R	8.2	7.7	16.9	9.2	9.5	N.D.	39
1/19 /7	82	M	L	---	7.6	19.6	16.1	---	20	20
	101	P	L	---	8.4	15.5	14.3	---	N.D.	25
	82	M	R	9.1	7.0	18.0	14.8	10.0	N.D.	20
10/27/76	43	P	L	---	18.9	39.9	---	---	79.7	52
	56	M	R	17.8	9.5	34.6	---	18.7	49.1	32.5
1/26/77	36	P	R	---	10.0	56.45	---	---	50.6	27.5
2/9/77	43	P	R	---	13.0	71.0	---	---	65	28
2/23/77	45	M	L	7.7	5.6	28.37	17.4	13.9	32	20
	38	P	L	10.2	5.6	33.3	17.4	29.3	30	26
	45	M	R	7.0	5.1	25.9	15.8	12.7	30	26
	38	P	R	10.2	6.7	48.7	20.8	29.3	38	20
3/30/77	50	P	L	10.5	---	53.0	---	19.2	52.4	---
	67	M	L	10.5	- -	36.2	---	19.0	48.5	---
	67	M	R	4.73	---	16.3	---	8.9	N.D.	---
	50	P	R	11.9	---	60.1	---	21.8	57.0	---
4/13/77	45	P	L	10.9	7.0	43.0	11.7	19.2	59.5	52
4/22/77	46	P	L	---	6.0	32.4	10.2	---	32.5	30
	44	M	L	---	6.5	38.0	---	---	39.8	30
	46	P	R	---	7.3	39.4	12.4	---	40.2	30
2/2/77	22	P	R	7.4	7.4	79.8	---	10.2	32	32.5
4/6/77	22	P	L	6.13	---	64.4	---	7.8	46.1	---

N.D. – No damage
P   – Paramacula
M   – Macula
L   – Left eye
R   – Right eye
*   – Based on MVL threshold power. If MVL power was not available, then OVL threshold power was used.
MVL – Microscopically visible lesion
OVL – Ophthalmoscopically visible lesion
     Experimental threshold temperatures computed with equation 3.

65

TABLE A-8. THRESHOLD POWER, TEMPERATURE, AND LESION RADIUS FOR Nd-YAG LASER (1060 nm) EXPOSURE

Monkey	Image radius @ 1/e² point (µm)	Site	Eye	Corneal power (mW) OVL threshold	MVL threshold	Temperature of lesion center (°C) Model*	Using MVL power	Lesion radius (µm) for MVL threshold Model	Experiment
10-s radiation:									
5/13/77	98	M	L	---	53.0	69.87	28.5	150	---
6/1/77	70	M	L	47.8	36	58.4	40.5	80	59
6/22/77	98	P	L	22.5	22.5	24.1	25.9	54	74
	98	M	L	24.5	24.5	23.5	18.7	51.6	59
7/28/77	70	P	L	29.5	26.5	43.4	25.2	64.4	---
8/4/77	98	M	L	16.0	14.5	18.4	34.4	12.4	44.4
	70	P	L	20.5	25.5	30.6	70.2	61.9	44.4
	98	M	R	---	23.5	27.0	55.8	59.6	---
	70	P	R	21.0	---	31.3	---	63.8	---
9/13/77	115	P	L	36.0	---	37.6	---	---	---
	115	M	R	21.5	---	22.4	---	---	---
	115	P	R	22.5	---	23.4	---	---	---
12/6/77	120	M	L	95	---	84.3	---	---	---
30-ms radiation:									
6/1/77	70	M	L	---	200	98.84	125	56.1	66.6
8/4/77	70	P	L	---	28.0	28.5	73.9	20.3	66.6
	98	M	R	---	48.5	36.5	61.7	35.5	

P   - Paramacula
M   - Macula
L   - Left eye
R   - Right eye
*   - Based on MVL threshold power. If MVL power was not available, then OVL threshold power was used.
MVL - Microscopically visible lesion
OVL - Ophthalmoscopically visible lesion
N.D. - No damage
       Experimental threshold temperatures computed with equation 3.

Table A-9. NORMALIZED MEASURED TEMPERATURES IN THE MONKEY EYE (λ = 514.4 nm)

Monkey	Image radius θ 1/e² point (μm)	Site	Normalized maximum temperature rise		Ratio of maximum temperature of 1/e² radius to maximum center temp.	
			30ms	10s	30ms	10s
10/13/76	630 NS	M	0.29	0.75	0.08	0.43
	NM	P	0.13	0.38	-	-
10/22/76	440	M	0.27	1.11	0.25	0.6
	NM	P	0.34	1.06	0.26	0.59
10/27/76	57	M	1.6	1.1	0.42	0.65
	44 B,I	P	-	-	-	-
11/3/76	108	M	0.67	0.96	0.63	0.95
	99	P	0.92	1.4	0.68	0.87
11/8/76	101	M	1.8	2.2	0.5	0.85
	93	P	2.3	3.3	0.57	0.68
1/6/77	112	M	0.98	2.14	0.64	0.8
	88	P	0.4 c	1.0 d	0.67	0.88
1/19/77	82	M	1.2	2.12	0.84	0.93
	101	P	1.04	1.7	0.76	0.96
1/26/77	36	P	-	-	-	-
2/2/77	22 B	P	1.01	1.38	0.88	0.96
2/9/77	43 B	P	0.59	0.75	0.89	0.98
2/23/77	45	M	1.53	3.08	0.47	0.71
	38	P	1.7	3.1	0.66	0.75
3/30/77	67	M	0.63 BD	0.5	0.71	0.6
	50	P	1.26	2.27	0.27	0.77
4/6/77	22 B	P	0.5	1.17	0.9	0.97
4/13/77	45	P	1.34	1.67	0.68	0.9
4/22/77	44	M	1.61		0.75	0.83
	46	P	1.5	1.7		
9/20/77	390	M	0.09	0.83	0.3	0.43
	480	P	0.1	0.45	0.1	0.56
	12	M	2.5		0.84	

M	- Macula
P	- Paramacula
NS	- Nonsymmetrical
NM	- Not measured
B	- Eye blanched
I	- Beam scan wrong
c	- 0.88 from other data
d	- 1.2 from other data
BD	- Bad data

TABLE A-10. MODEL AND EXPERIMENTAL TEMPERATURES FOR NEODYMIUM EXPERIMENTS

Corneal power (mW)	Image size (1/e² rad.) (μm)	Center temp.(°C)		1/e² radius temp.(°C)	
		M	E	M	E
10-s radiation:					
9.8	120	8.5	3.1	4.3	2.8
36.0	115	37.5	30	18	24.5
45.0	175	15	38	5	
25.0	175	17.5	34	7.5	19
25	70	37	33	19	25
16.0	98	18.5	28.8	7.5	25
20.5	70	30	52.6	15	43
29.5	70	43	22	1.	21
24.5	98	23.5	21	9.5	14.6
22.5	98	24	18	11.0	12.5
8.4	70	13.5	9.5	4.8	6.4
11.0	88	74	32	38	30
30-ms radiation:					
45.0	70	46	30	15.6	19
48.5	98	36	60	7.0	36.5
28.0	70	28	40	10.2	25
80.0	70	98	50	23	32
36	88	31	24.2	7.8	17.2
36	88	31	4 2	-----Bad run-----	

M - model

E - experiment

TABLE A-11. COMPARISON OF RIGHT- AND LEFT-EYE ARGON-THRESHOLD CORNEAL POWERS

Site	Irradiation time (s)	Threshold corneal power (mW)		RE/LE	Image radius (μm)	Lesion radius	
		RE	LE			RE	LE
P	0.03	33.0			72	20	
P	10	7.4			43.4	33	
P	0.03	20.3			43.4	13	
P	10	13.0			86.8	27.5	
P	0.03	41.3			86.8	20	
M	10	5.1	5.6	0.91	89.6	26	20
M	0.03	16.8	13.3	1.26	89.6	20	20
P	10	6.7	5.6	1.2	75.6	20	26
P	0.03	12.6	28	0.45	75.6	20	26
P	0.03	31.5	35	0.9	101		
P	10	11.9	10.5	1.13	101		
M	10	4.73	10.5	0.45	134.4		
M	0.03	23.8			13.4		
P	10		6.13		44		
P	0.03		9.1		44		
P	10		7.0		90		52
P	0.03		42		90		78
M	0.03		10.9		88		35
M	10	7.3	6.5	1.12	88	30	30
P	0.03	23.8	11.9	2.0	92	60	30
P	10		6.0		92		30

P - Paramacular
M - Macular
RE/LE - Ratio of threshold corneal powers of right eye with respect to left eye

TABLE A-12. THRESHOLD CORNEAL POWERS THAT PRODUCE LESION RADII BETWEEN 20 and 40 μm (λ = 514.5 nm)

Experiment	Image 1/e² radius (μm)	Site	Model corneal power (30-μm radius) 0.03 s	Model corneal power (30-μm radius) 10 s	Experimental corneal power (20–40-μm radius) 0.03 s L	Experimental corneal power (20–40-μm radius) 0.03 s R	Experimental corneal power (20–40-μm radius) 10 s L	Experimental corneal power (20–40-μm radius) 10 s R
10/13/76	630	P	356	63				
10/22/76	440	P	180	41	141		130	20
10/27/76	43	P	22	10	74 B	77		10
11/3/76	108	M	25	11			6.3	
	99	P	26	11	28		8.8	
11/8/76	101	M	24	10.5	16.8		4.0	4.6
	92	P	20	9	15.8		4.6	7.7
1/6/77	112	M	29	13	40.3	42	7	
	87	P	23	10	33	38	7.4	
1/19/77	82	M	19	8.5		35	7.6	7.0, 4.6
	101	P	28	12	48	33	8.4	
1/26/77	36	P	12	6.0		33		10
2/2/77	22	P	17	7.5		20.3		7.4
2/9/77	43	P				41		13
2/23/77	45	M	12	6.0	13.3	12.6	5.6	5.1
	38	F	12	5.6	28	12.6	5.6	6.7
4/23/77	44	M	10.5	5.0	10.9		6.5	
	46	P	12	5.8	11.9		6.0	7.3

L - Left eye
R - Right eye
B - Eye blanched
P - Paramacular
M - Macular

APPENDIX B

MEASUREMENT OF RETINAL INTENSITY PROFILE WITH MICROSENSORS

The measurement of light intensity with a thermocouple or fiber optic represents, at best, the average power of the light over the surface of the sensor. Whenever the sensor area is large with respect to the light image, measurement errors occur. The magnitude of these errors can be estimated by modeling the sensor surface as a disc and assuming that the sensor measures the average power of light striking its surface.

Consider the problem of measuring the radial, relative intensity profile of a circular, symmetric, unimodal image produced by a laser. Typically, the measurement is made by scanning the sensor across the image and plotting the output of the sensor (Fig. B-1).

If the radial intensity profile of the laser image is $I(r)$, the probe measurement may be estimated by computing the integral of $I(r)$ over the surface of the probe. To obtain a numerical value of this integral, assume the profile is Gaussian. The complexity of the computation may be reduced by placing the probe at the center of the coordinate system and moving the profile with respect to a fixed probe. When the image is centered at the origin, its intensity distribution is

$$I(r) = k\ e^{-\frac{1}{2}\frac{r^2}{\sigma^2}} = k\ e^{-\frac{1}{2}\frac{(x^2+y^2)}{\sigma^2}}$$

When the image center is displaced a distance c along the x axis from the origin, the image intensity becomes

$$I(x,y) = k\ e^{-\frac{1}{2}\frac{[(x-c)^2+y^2]}{\sigma^2}}$$

The total power on the probe is given by

$$P = 2 \int_{y=0}^{R} \int_{x=-\sqrt{R^2-y^2}}^{x=+\sqrt{R^2-y^2}} k\ e^{-\frac{1}{2}\frac{[(x-c)^2+y^2]}{\sigma^2}}\ dx\ dy$$

The integral is numerically evaluated by dividing the surface of the sensor into a number of squares and assuming that the power in each square is equal to area of the square times intensity of the image at the center of the square. The size of the square required for accurate evaluation of the integral can be determined by numerically evaluating the integral as a function of incremental
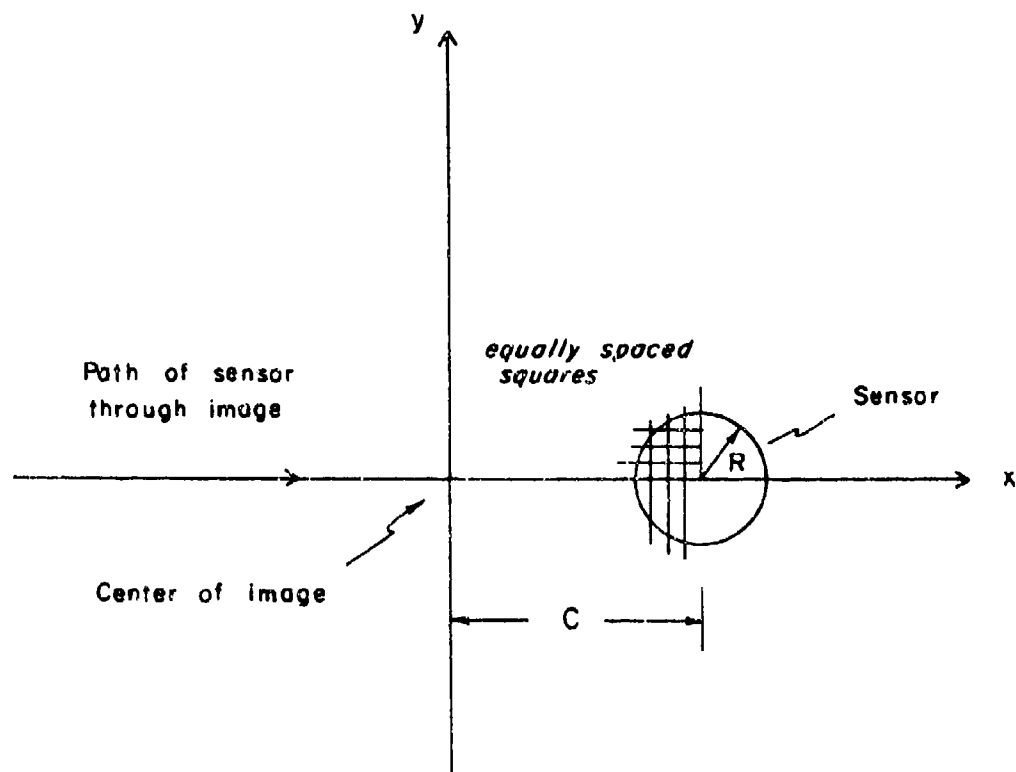
Figure B-1. Geometry for measuring relative intensity profile with a thermocouple or fiber-optic sensor.

area and comparing the solutions with the analytic solution of the integral when the image is cente d at the origin. For $c = 0$ the power on the probe is

$$P = 2\pi \int_0^R k \, e^{-\frac{1}{2}\left(\frac{r}{\sigma}\right)^2} r \, dr$$

$$= 2\pi k \sigma^2 \left(1 - e^{-\frac{1}{2}\frac{R^2}{\sigma^2}}\right)$$

In Figure B-2, computed relative intensity profiles for probe radii of 5 and 10 µm are compared to the radial profile of a Gaussian distribution with a standard deviation of 10 µm. The incremental area for these computations was $(R/1000)^2$. Even when the probe radius was equal to the standard deviation of the image, the measured profile was only 11% too large. These results indicate that the sizes of the sensors used by The University of Texas have not introduced error into the measurement of intensity profiles in the eye. It should be possible to accurately measure point and line spread functions in the eye with a 5-µm probe.
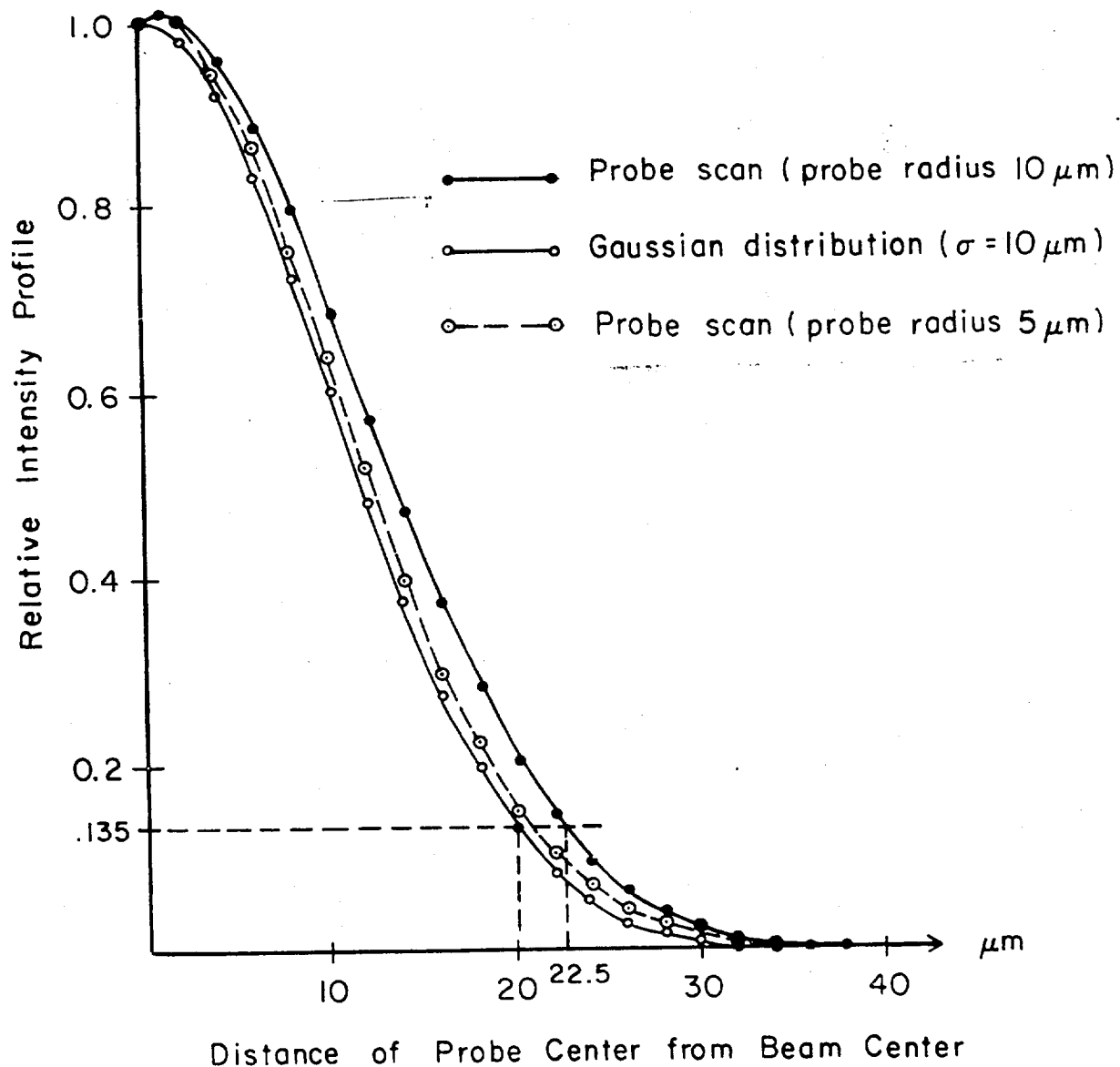

Figure B-2. Calculated relative intensity profiles measured by 5- and 10-µm-radius sensors of a Gaussian beam, with standard deviation of 10 µm.